nature communications

Article

https://doi.org/10.1038/s41467-024-50900-1

# Extraordinary phase transition revealed in a van der Waals antiferromagnet

Received: 28 August 2023

Accepted: 22 July 2024

Published online: 31 July 2024

Check for updates

Xiaoyu Guo[1,8], Wenhao Liu[2,8], Jonathan Schwartz[3], Suk Hyun Sung[3], Dechen Zhang[1], Makoto Shimizu[4,7], Aswin L. N. Kondusamy[2], Lu Li[1], Kai Sun[1], Hui Deng[1], Harald O. Jeschke[5], Igor I. Mazin[6], Robert Hovden[3], Bing Lv[2] ✉ & Liuyan Zhao[1] ✉

While the surface-bulk correspondence has been ubiquitously shown in topological phases, the relationship between surface and bulk in Landau-like phases is much less explored. Theoretical investigations since 1970s for semi-infinite systems have predicted the possibility of the surface order emerging at a higher temperature than the bulk, clearly illustrating a counterintuitive situation and greatly enriching phase transitions. But experimental realizations of this prediction remain missing. Here, we demonstrate the higher-temperature surface and lower-temperature bulk phase transitions in CrSBr, a van der Waals (vdW) layered antiferromagnet. We leverage the surface sensitivity of electric dipole second harmonic generation (SHG) to resolve surface magnetism, the bulk nature of electric quadrupole SHG to probe bulk spin correlations, and their interference to capture the two magnetic domain states. Our density functional theory calculations show the suppression of ferromagnetic-antiferromagnetic competition at the surface is responsible for this enhanced surface magnetism. Our results not only show counterintuitive, richer phase transitions in vdW magnets, but also provide viable ways to enhance magnetism in their 2D form.

Surfaces are always present in practical materials. Even in macroscopic materials, the presence of surfaces has the potential to enrich their phase diagrams of spontaneous symmetry breaking phases[1–4]. Taking magnets as an example, in the temperature ($T$) versus surface-to-bulk relative exchange interaction ($J_s/J_b$) phase diagram shown in Fig. 1a, three distinct phase transitions were theoretically identified, namely "ordinary", "surface", and "extraordinary" transitions. The typical transition, where the surface and the bulk order simultaneously, is called "ordinary", and the one when the surface orders, but the bulk does not, is a "surface" transition. The transition establishing the bulk order in the presence of the surface order is called "extraordinary". The point where three different phases meet is a "special point". In the "ordinary" case when $J_s$ is much weaker than $J_b$, the bulk order generates an effective field to induce a finite order at the surface, and thus the system undergoes only a single phase transition. Conversely, in the "surface" and "extraordinary" cases with $J_s$ much greater than $J_b$, the surface order cannot provide a notable effective field deep in the inner bulk, and thus, the bulk undergoes a separate "extraordinary" phase transition, leading to the split into two phase transitions.

Separation of an ordinary phase transition into surface and extraordinary ones is highly uncommon, and requires that interactions responsible for the ordering are enhanced at the surface compared to

[1]Department of Physics, University of Michigan, Ann Arbor, MI, USA. [2]Department of Physics, the University of Texas at Dallas, Richardson, TX, USA. [3]Department of Materials Science and Engineering, University of Michigan, Ann Arbor, MI, USA. [4]Department of Physics, Okayama University, Okayama, Japan. [5]Research Institute for Interdisciplinary Science, Okayama University, Okayama, Japan. [6]Department of Physics and Astronomy, and Quantum Science and Engineering Center, George Mason University, Fairfax, VA, USA. [7]Present address: Department of Physics, Graduate School of Science, Kyoto University, Kyoto, Japan. [8]These authors contributed equally: Xiaoyu Guo, Wenhao Liu. ✉e-mail: blv@utdallas.edu; lyzhao@umich.edu

https://doi.org/10.1038/s41467-024-50900-1

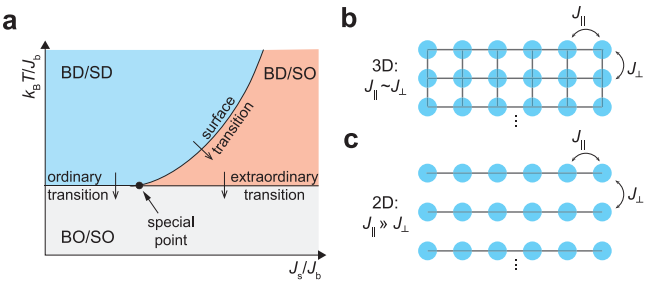


**Fig. 1 | vdW materials are promising platforms for hosting surface and extraordinary phase transitions. a** phase diagram illustrating ordinary, surface and extraordinary phase transitions and the special point. BD bulk disordered, SD surface disordered, SO surface ordered, BO bulk ordered. $J_s$, mean-field surface interaction, $J_b$, mean-field bulk interaction. **b**, **c** illustrations of intralayer and interlayer interactions strengths, $J_{||}$ and $J_{\perp}$, in **b** 3D ionic crystals and **c** quasi-2D van der Waals crystals.

the bulk. In three dimensional (3D) magnetic materials where the interaction between sites within the plane (intralayer interaction $J_{||}$) is comparable to that for sites between the neighboring planes (interlayer interaction $J_{\perp}$), the mean-field coupling at the surface ($J_s$), being the sum of all interactions, is expected to be smaller than the one inside the bulk ($J_b$) because of the loss of a $J_{\perp}$ contribution from a neighboring layer (Fig. 1b). For such 3D materials, it is unlikely that any minor surface modifications could compensate for the missing $J_{\perp}$ that is of similar strength as $J_{||}$. On the other hand, in quasi-two-dimensional (2D) materials where $J_{||}$ is much larger than $J_{\perp}$ (Fig. 1c), it becomes possible that small changes in the surface layers could make up for the very weak missing $J_{\perp}$, or even push its mean-field coupling strength beyond the bulk one to overcome the reduction due to stronger fluctuations at the surface. Therefore, quasi-2D materials, such as van der Waals (vdW) materials, are potential material platforms for realizing split surface-extraordinary phase transitions. Yet, the research on vdW and 2D materials in the past couple of decades hardly revealed any viable candidates for such splitting.

One major challenge for detecting surface and extraordinary phase transitions is the lack of experimental tools sensitive to phase transitions both at the surface and inside the bulk. The leading order electric dipole (ED) contribution to second harmonic generation (SHG) is known as an excellent probe for the broken spatial inversion symmetry and has been used extensively to investigate surface properties[5–9]. Very recently, the next order electric quadrupole (EQ) and magnetic dipole (MD) contributions to SHG have been successfully detected in many spatial-inversion-symmetric materials[10–13] and further emerged as an important tool for revealing centrosymmetric bulk phase transitions[14–19]. The combination of ED and EQ/MD contributions to SHG is a suitable tool for an experimental discovery of surface and extraordinary phase transitions.

The material candidate selected for this study is CrSBr, a vdW layered crystal with an orthorhombic point group (*mmm*). The structural primitive cell contains two edge-sharing distorted octahedra, with Cr at the center and S/Br at the vertices, forming an in-plane (*ab*-plane) orthorhombic network and stacking vertically along the out-of-plane (*c*-axis) direction[20,21]. Bulk CrSBr exhibits four characteristic temperatures: $T^* = 185$ K[22] and $T^{**} = 155$ K[21–24] for two crossovers for the enhanced local dynamic spin correlations, $T_N = 132$ K for the onset of bulk layered antiferromagnetic (AFM) order[20–27], and $T_F = 30$–$40$ K for the formation of a possible ferromagnetic (FM) state with debated origins[24,26,28]. The layered AFM features a FM spin alignment along the *b*-axis within each atomic layer and an AFM coupling between adjacent layers along the *c*-axis. The magnetic point group is $mmm1'$ for the bulk AFM order where the *c*-axis translational symmetry is present and $m'm2'$ for the surface order where the out-of-plane translational

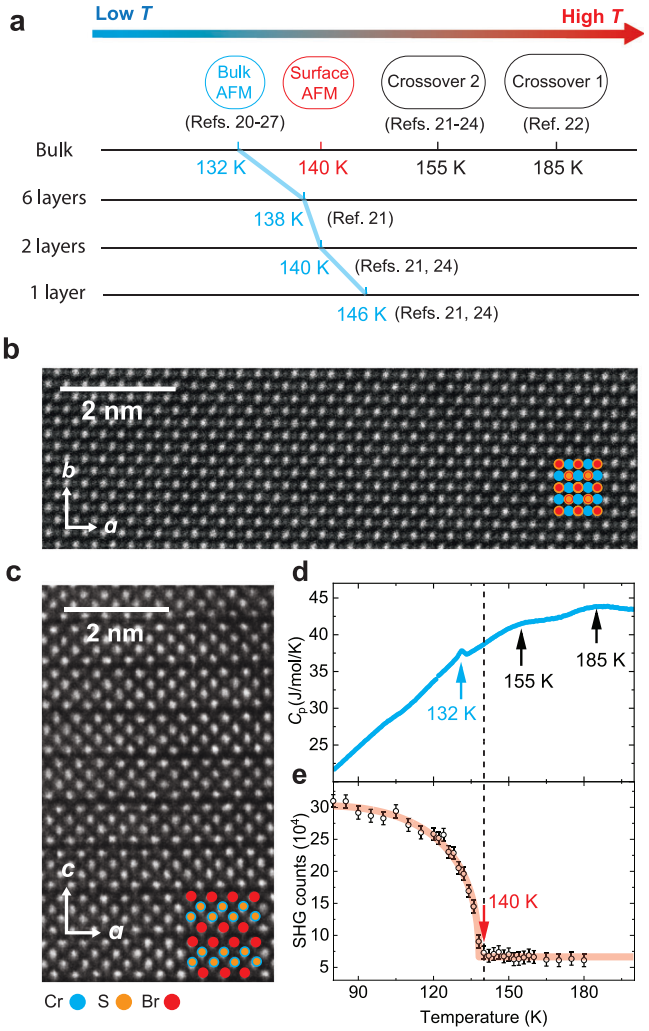


**Fig. 2 | STEM, heat capacity, and SHG characterizations of CrSBr bulk crystals.** **a** summary of magnetic phases and corresponding characteristic temperatures in bulk and few-layer CrSBr from the literature. **b** plan- and **c** side-view atomically resolved HAADF-STEM images of the CrSBr crystal, confirming the scarcity of atomic and stacking defects. **d** temperature dependent specific heat result showing the three reported characteristic temperatures, $T^* = 185$ K, $T^{**} = 155$ K, and $T_N = 132$ K. **e** temperature dependent SHG intensity in the $S_{in}$-$S_{out}$ channel at the angle $\phi = 40^\circ$ revealing an onset at 140 K for 3D bulk CrSBr, different from the bulk $T_N = 132$ K. The red curve serves as a guide to the eyes. Error bars indicate the noise level of each SHG measurement.

symmetry is absent. Interestingly, the onset of layered AFM occurs at different temperatures for CrSBr of different thicknesses: 138 K for six-layer CrSBr, 140 K for bilayer CrSBr and the FM order onsets at possibly 146 K for monolayer CrSBr[21]. This monotonic increase of the magnetic onset temperature with the decreasing thickness in CrSBr starkly contrasts with nearly all known vdW magnets, such as $CrI_3$[29,30], $Cr_2Ge_2Te_6$[31], $Fe_3GeTe_2$[32], $NiPS_3$[33], $FePS_3$[34,35], $MnPSe_3$[36], etc., where the magnetic onset temperature in few-layer samples is either lower or equal to that of the bulk crystals.

Figure 2a summarizes the magnetic characteristic temperatures in CrSBr of different thicknesses that are probed by different experimental techniques. It can be seen that eliminating all neighboring layers, i.e., transitioning from bulk to monolayer, leads to an increase in the critical temperature by possibly about 14 K, and that keeping only one neighboring layer, i.e., going from bulk to bilayer, results in an increment of 8 K, close to half of the 14 K increment above. In addition, the Néel temperature of 138 K for six-layer CrSBr is comparable to the

https://doi.org/10.1038/s41467-024-50900-1

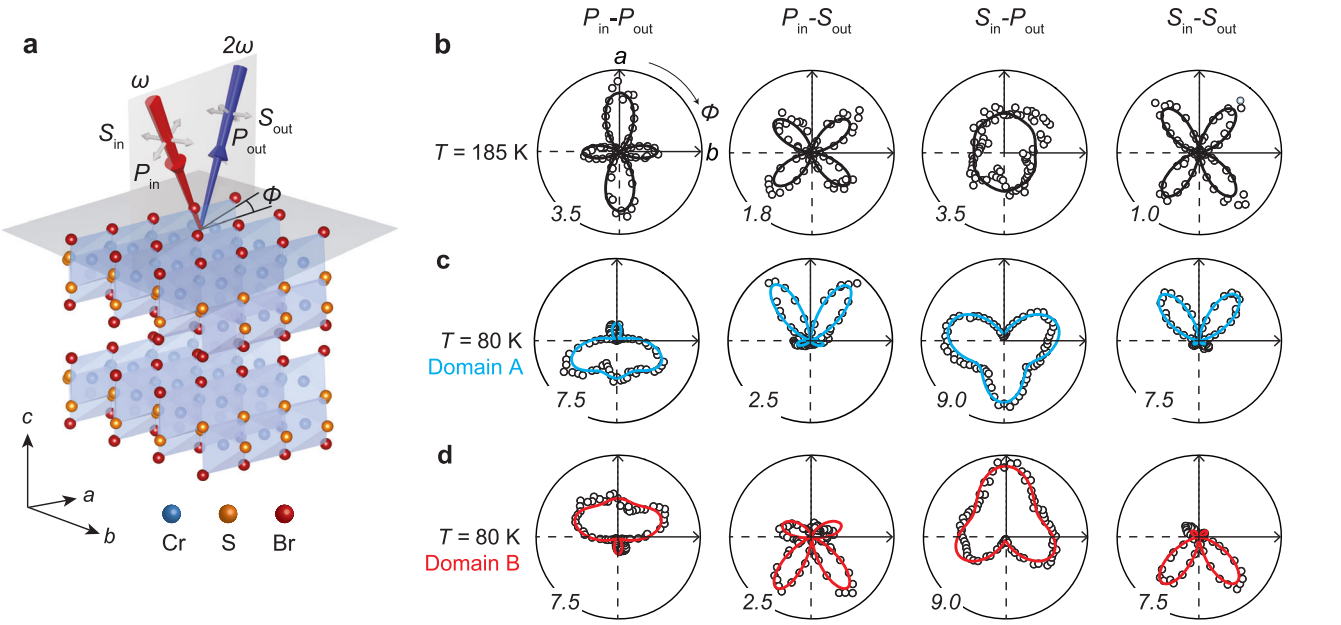


**Fig. 3 | SHG RA revealing two degenerate magnetic domain states. a** schematic of the oblique incidence SHG RA measurement taken on a bulk CrSBr crystal. Red arrow: incident fundamental light, blue arrow: outgoing SHG light, gray arrows: light polarizations, $\omega$, frequency of the incident light. **b**–**d** SHG RA polar plots in four channels ($P/S_{in}$-$P/S_{out}$) at **b** 185 K, **c** 80 K from domain A and **d** 80 K from domain B. Experiment data (circles) are fitted by functional forms simulated based on group theory analysis (solid curves). Numbers at the corners indicate the scales of the polar plots, with 1.0 corresponding to 1 fW.

average temperature of two bilayers and four bulk layers, i.e., $(2T_N^{bilayer} + 4T_N^{bulk})/6 = 135$ K. Such considerations motivate us to investigate the surface of bulk CrSBr, closely resembling the bilayer case with only one neighboring layer, to search for the extraordinary and surface phase transitions.

In this work, using temperature-dependent oblique incidence SHG rotation anisotropy (RA), we reveal a higher-temperature surface and a lower-temperature bulk "extraordinary" phase transition in 3D CrSBr single crystals.

## Results

### STEM, transport, and SHG charaterizations of 3D CrSBr crystals

vdW materials often suffer from atomic defects and stacking faults that potentially affect their electronic and magnetic properties[37–40]. To assess the crystallographic quality of our bulk CrSBr, we performed high-angle annular dark-field scanning transmission electron microscopy (HAADF-STEM) measurements in both plan-view and cross-section-view configurations (see Methods). Figure 2b shows the atomic structure of CrSBr within the *ab*-plane, with the Br/S column appearing to be the brightest, followed by a dimmer Cr column. Across multiple sites and samples of various thicknesses, atomic defects were rarely observed in the plan-view STEM images of CrSBr. Figure 2c displays the layered structure of CrSBr viewed in the *ac*-plane, with the vdW gaps showing up as the darker space between atomic layers. We further confirm that the overlying interlayer stacking is the sole preferred stacking geometry for CrSBr and barely any stacking faults were observed across multiple sites (see Supplementary Note 1). This scarcity of atomic defects and stacking faults confirms the high crystalline quality of our CrSBr samples (see Methods for growth method). Our atomic force microscopy measurements also show that our freshly cleaved surfaces exhibit highly flat surfaces with a low density of atomic steps (see Supplementary Note 2).

The temperature-dependent heat capacity for single-crystalline CrSBr samples clearly reproduces the three temperature scales reported in the literature, $T^* = 185$ K, $T^{**} = 155$ K, and $T_N = 132$ K (Fig. 2d), whereas $T_F = 30$ K is revealed by the magnetization measurement (see Supplementary Note 3). Intriguingly, the temperature dependence of the SHG intensity from the same CrSBr batch exhibits a clear order-parameter-like upturn at 140 K (Fig. 2e), a temperature that is hidden to many bulk-sensitive measurements for 3D CrSBr single crystals, for example, heat capacity[21,22], magnetic susceptibility[20,22,24,26–28], neutron single crystal diffraction[23], and zero-field $\mu$SR[26]. We note that, first, unlike $T_N = 132$ K for 3D CrSBr single crystals, neutron diffraction experiments on CrSBr powders that have a substantial surface to bulk ratio[26] showed $T_N = 140$ K and, second, SHG revealed $T_N = 140$ K for bilayer CrSBr whose composing layers miss the neighboring layer on one side[21]. The occurrence of the same critical temperature 140 K in bulk single crystals of this study, together with the surface sensitivity of the ED SHG probe[5–9,41,42], indicates that this 140 K onset in bulk CrSBr crystals is likely the surface ordering temperature $T_S = 140$ K, which is higher than the bulk Néel temperature, $T_N = 132$ K, but lower than the crossover temperature, $T^{**} = 155$ K (Fig. 2a).

### Oblique incident SHG RA tracking phase transitions in 3D CrSBr crystals

To analyze further the magnetic phase transitions in bulk CrSBr crystals, we performed the rotation anisotropy (RA) measurements of SHG at an oblique incident angle $\theta$, to capture the symmetry evolution across the critical temperatures. In a SHG RA measurement (Fig. 3a), the intensity of reflected SHG light is recorded as a function of the azimuthal angle $\phi$ between the crystal axis $a$ and the light scattering plane in one of the four polarization channels, $P/S_{in}$-$P/S_{out}$, with $P/S_{in/out}$ standing for the incident/outgoing light polarization selected to be parallel/perpendicular to the light scattering plane. We start by showing SHG RA data taken at high temperatures ($T \geq T^*$), specifically at 185 K (Fig. 3b) and 295 K (see Supplementary Note 4), that are nearly identical in both the RA patterns and the SHG intensity in all four polarization channels. The four SHG RA polar plots in Fig. 3b are two-fold rotational symmetric about the *c*-axis ($C_{2c}$) and mirror symmetric with mirrors normal to the *a*- and *b*-axis ($m_a$ and $m_b$). They are well fitted by the EQ contribution to the SHG under the centrosymmetric point group *mmm*. We exclude the surface ED, bulk MD, and electric field-induced SH contributions as primary sources, even if present, for our SHG RA data at $T \geq T^*$ (Supplementary Note 4).

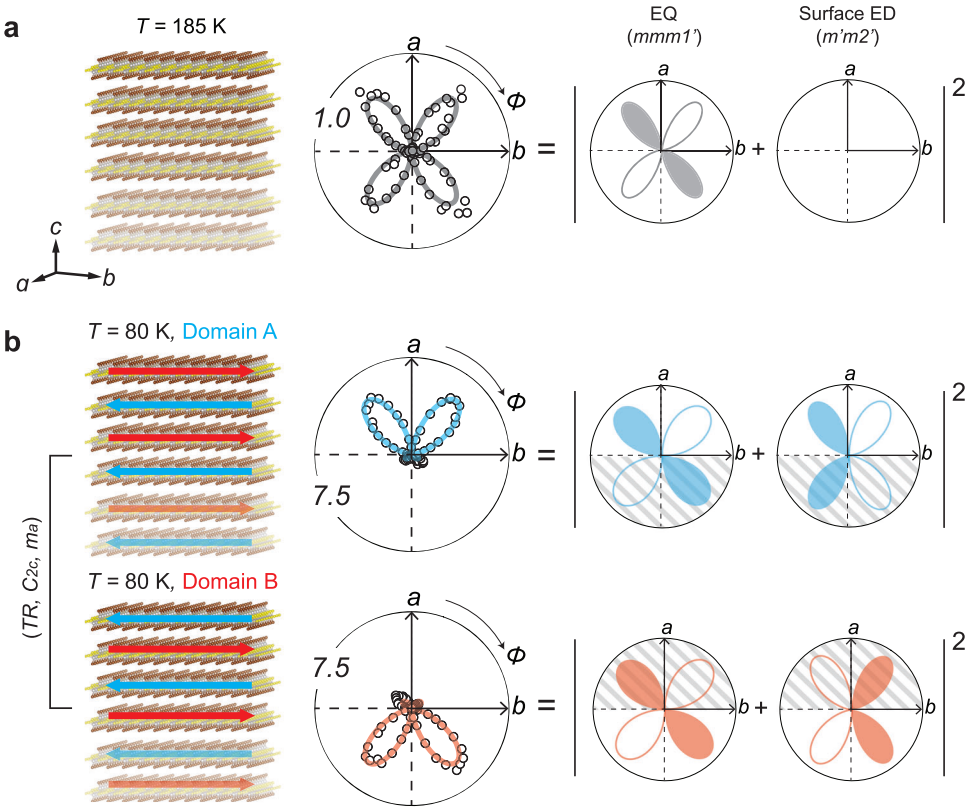


**Fig. 4 | Interference between bulk EQ and surface ED leading to distinct SHG RA patterns for the two domain states. a** left: schematic of the layered crystal structure at 185 K. Right: SHG RA pattern in the $S_{in}$-$S_{out}$ channel with only the EQ contribution. **b** left: schematic of the layered crystal structure overlaid with the spin texture in domain states A and B, related by the time-reversal operation (*TR*), two-fold rotation along the *c*-axis ($C_{2c}$) and mirror operation perpendicular to the *a*-axis ($m_a$). Right: SHG RA patterns in the $S_{in}$-$S_{out}$ channel, resulting from the interference between the bulk EQ and the surface ED contributions. The colored shaded areas of the SHG RA patterns indicate a $\pi$ phase shift of the SHG electric field from the white shaded areas. Stripped shaded areas indicate destructive interference. Numbers at the corners indicate the scales of the polar plots, with 1.0 corresponding to 1 fW. EQ electric quadrupole, ED electric dipole.

Upon cooling to low temperatures ($T < T_N$), we observe two, and only two distinct types of SHG RA data at 80 K through measurements across multiple thermal cycles and in different samples, as shown in Fig. 3c, d. Contrary to the RA patterns at 185 K, the SHG RA patterns at 80 K evidently break the $C_{2c}$ and $m_a$ symmetries but retain the $m_b$ symmetry. The comparison between Fig. 3c, d demonstrates that the two types of SHG RA data are related by either a $C_{2c}$ or a $m_a$ operation, which are the symmetries broken below $T_N$, and therefore, confirms that they correspond to the two degenerate magnetic domain states, $\leftarrow\rightarrow\leftarrow\rightarrow\ldots$ (Domain A) and $\rightarrow\leftarrow\rightarrow\leftarrow\ldots$ (Domain B), where $\leftarrow/\rightarrow$ represents the spins within individual layers aligning along the negative/positive direction of the *b*-axis. A real-space survey of SHG RA across a CrSBr single crystal surface shows that the domain size extends up to 500 μm (see Supplementary Note 5), and a survey conducted over several thermal cycles demonstrated the random selection of domain states in individual thermal cycles (see Supplementary Note 5).

To model and fit the SHG RA data at low temperatures, we need to identify the SHG radiation sources and their corresponding point groups. Firstly, due to the absence of reported structural transitions for CrSBr within our temperature range of interest (80–295 K)[26], the EQ contribution to SHG based on the structural point group *mmm* ($\chi^{EQ,s}_{ijkl}$) should be present at all temperatures. Secondly, due to the centrosymmetric and time-invariant bulk layered AFM order that sets in below $T_N = 132$ K, the EQ contribution to SHG from the magnetic point group *mmm*1′ ($\chi^{EQ,bAFM}_{ijkl}$) should be considered at temperatures below $T_N$. We notice that the symmetry constraints are the same for the structural point group *mmm* and the magnetic point group *mmm*1′, resulting in that $\chi^{EQ,s}_{ijkl}$ is of the same form as $\chi^{EQ,bAFM}_{ijkl}$. Hence, from this point onward, we use $\chi^{EQ}_{ijkl}$ to represent the combined contributions from the structure and the bulk AFM. Thirdly, the surface layered AFM breaks the spatial inversion and time reversal (*TR*) symmetries, and as a result, the ED contribution to SHG from the surface magnetic point group *m*′*m*2′ ($\chi^{ED}_{ijk}$) should be included at low temperatures $T < T_S$. Therefore, the SHG RA data at 80 K should be modeled by a coherent superposition of the EQ and the ED contributions (see Supplementary Note 6 and Methods) and thus, is capable of probing the magnetic phase transition at the surface. The fitted results based on this model are depicted in Fig. 3c, d, and the interference between the EQ and ED contributions is illustrated for the $S_{in}$-$S_{out}$ polarization channel in Fig. 4. Moreover, the thickness dependent SHG RA measurements below $T_N$ show an increasing trend of the EQ SHG contribution, but a constant level of the ED SHG contribution with increasing sample thickness, which is consistent with their assigned bulk and surface origins, respectively (see Supplementary Note 7).

Figure 4a confirms the sole presence of the EQ contribution to SHG at $T = 185$ K. More interesting is that Fig. 4b shows distinct consequences between the two domain states from the interference of the bulk EQ and the surface ED contributions: constructive interference in the top half and destructive interference in the bottom half for Domain A, and the exact opposite way for Domain B. The bulk AFM order preserves all the symmetry operations in the structural point group and the *TR* operation, resulting in $\chi^{EQ}_{ijkl}$(Domain A) = $\chi^{EQ}_{ijkl}$ (Domain B). The surface AFM order however breaks $C_{2c}$, $m_a$, and *TR* symmetries that relate the two domain states, leading to $\chi^{ED}_{ijk}$(Domain A) = $-\chi^{ED}_{ijk}$(Domain B) (see Supplementary Note 6). This opposite sign relationship between the EQ and ED SHG susceptibilities for the two domain states explains the distinct interference behaviors observed in Fig. 4b.

https://doi.org/10.1038/s41467-024-50900-1

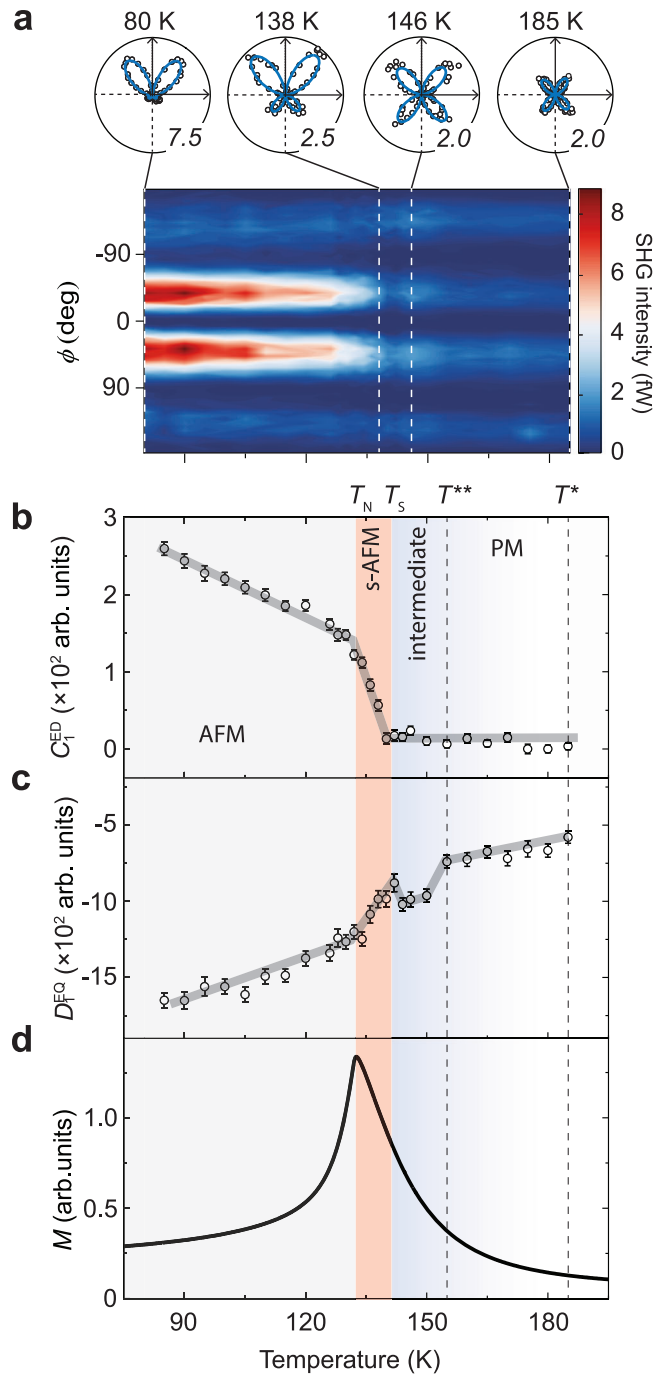


**Fig. 5 | Temperature-dependent SHG RA revealing the surface and the extraordinary phase transitions. a** lower: contour plot of the SHG RA in the $S_{in}$-$S_{out}$ channel as a function of temperature. Upper: SHG RA polar plots in the $S_{in}$-$S_{out}$ channel at four selected temperatures. **b** The electric dipole (ED) coefficient $C_1^{ED}$ and (**c**) the electric quadrupole (EQ) coefficient $D_1^{EQ}$ as a function of temperature. Gray curves serve as guides to the eyes. The temperature dependent SHG data were collected during the warming up cycle. **d** magnetization as a function of temperature measured under 1000 Oe magnetic field along the *b*-axis. The regions of paramagnetism (PM), intermediate magnetic crossover (intermediate), surface antiferromagnetism (s-AFM) and bulk antiferromagnetism (AFM) are shaded in different colors, with their characteristic temperatures marked. Error bars indicate the standard deviation from the fitting.

Our next step is to track the magnetic phase transitions by performing careful temperature dependent SHG RA measurements, paired with magnetization measurements on the same CrSBr crystal. During SHG measurements, we ensure our system is in thermal equilibrium by keeping a slow heating rate, waiting for additional time after the temperature is stabilized (see Methods), and noticing no SHG pattern change as a function of time (see Supplementary Note 8 for SHG RA patterns measured in sequence of time). Figure 5a shows a color map of SHG intensity taken in the $S_{in}$-$S_{out}$ channel as functions of the azimuthal angle $\phi$ and the temperature $T$. A horizontal linecut at a fixed $\phi_0$ yields the temperature-dependent SHG intensity, such as the trace shown in Fig. 2e, whereas the vertical linecut at a selected $T$ gives the SHG RA pattern, such as the polar plots shown in Fig. 4. To better visualize the evolution of the SHG RA data as the temperature decreases, we present polar plots at four representative temperatures in the inset of Fig. 5a: $T = 185$ K (around $T^*$), 146 K (between $T^{**}$ and $T_S$), 138 K (between $T_S$ and $T_N$), and 80 K (below $T_N$). A clear trend can be observed: the RA pattern first increases in the SHG intensity but retains the pattern shape of four even lobes until $T_S$. It then exhibits two pairs of uneven lobes while further amplifying the intensity of the larger and reducing the intensity of the smaller pair below $T_S$. As the temperature decreases below $T_N$, a more pronounced contrast in the SHG intensity between the larger and smaller pairs of lobes is developed.

The SHG RA pattern at every temperature in Fig. 5a is fitted by the coherent superposition of the surface ED and the bulk EQ contributions to extract the temperature dependence of their sources (see Methods for the fitting procedure). For the $S_{in}$-$S_{out}$ channel, the fitted results include two independent parameters for the surface ED source, $C_1^{ED} = \chi_{xyy}^{ED} + 2\chi_{yxy}^{ED}$, and $C_2^{ED} = \chi_{xxx}^{ED}$, and another two for the bulk EQ one, $D_1^{EQ} = \chi_{xxxx}^{EQ} - 2\chi_{xxyy}^{EQ} - \chi_{yxyx}^{EQ}$, and $D_2^{EQ} = \chi_{xyxy}^{EQ} + 2\chi_{yyxx}^{EQ} - \chi_{yyyy}^{EQ}$. Because $\chi_{ijk}^{ED}$ is variant and $\chi_{ijkl}^{EQ}$ is invariant under the *TR* operation, we know that $\chi_{ijk}^{ED}$ is proportional to the odd powers of the Néel vector (**N**) and $\chi_{ijkl}^{EQ}$ scales with the even powers of **N**. Under the leading-order approximation, $\chi_{ijk}^{ED} \propto \mathbf{N}$ and $\chi_{ijkl}^{EQ} \propto$ constant + **N**·**N**, and as a result, $C_{1,2}^{ED} \propto \mathbf{N}$ and $D_{1,2}^{EQ} \propto$ constant + **N**·**N**. Figure 5b, c shows the temperature dependence of $C_1^{ED}$ and $D_1^{EQ}$ (see $C_2^{ED}$ and $D_2^{EQ}$ in Supplementary Note 9), and Fig. 5d displays the temperature dependence of the bulk magnetization of the same CrSBr crystal. The bulk magnetization $M$ clearly shows a divergent behavior at $T_N = 132$ K, as expected for a bulk CrSBr crystal[20–27]. Three important temperature scales are captured in the temperature dependence of ED and EQ contributions, $T^{**} = 155$ K, $T_S = 140$ K, and $T_N = 132$ K that are discussed in-depth below (see Supplementary Note 10 for data from another sample). The surface ED contribution $C_1^{ED}(T)$, which is proportional to **N**, shows an order-parameter-like onset at $T_S = 140 \pm 0.2$ K and then an observable kink at $T_N = 132$ K. This observation confirms that the surface orders antiferromagnetically at a higher temperature than the bulk, providing definitive evidence for a surface phase transition in bulk CrSBr. The kink behavior at $T_N = 132$ K reflects the impact of the bulk extraordinary phase transition on the surface order, which is consistent with the theoretical prediction of an $\beta$>1 critical exponent for the surface order parameter at the extraordinary phase transition temperature[4,43]. The EQ part $D_1^{EQ}(T)$, which scales with **N**·**N** after a constant offset from the structural contribution, initially experiences a steady but slow increase below $T^* = 185$ K until $T^{**} = 155$ K. Subsequently, it increases steeply across $T^{**}$, exhibits a notable peak at $T_S = 140$ K, and ultimately a kink at $T_N = 132$ K. Note that the EQ SHG probes CrSBr within the light penetration depth, which includes and goes beyond the surface depth. Provided its sensitivity to the spin correlation via the term **N**·**N**, it shows a weak divergence, i.e., the peak, at $T_S$, as well as the slope change across $T^{**}$.

To understand these three observed temperature scales, we compare them with the literature reported ones for CrSBr of bulk, powder, and film forms. First, our bulk AFM order onset temperature, $T_N = 132$ K, is consistent with that of bulk CrSBr single crystals measured by single crystal neutron diffraction, $\mu$SR, heat capacity, and magnetic susceptibility[20–27]. Second, our surface AFM order onset

temperature, $T_S = 140 \pm 0.2$ K, coincides with the magnetic critical temperature reported for powder CrSBr measured with powder neutron diffraction[26] and bilayer CrSBr with SHG[21]. For powder CrSBr, the surface-to-bulk ratio is significantly increased from that of single crystal CrSBr, and thus, it might be possible that the powder neutron diffraction is sensitive to the surface magnetism. For bilayer CrSBr, it resembles the surface magnetism in 3D CrSBr in the way that they both miss neighboring layers on one side. Therefore, our detection of $T_S = 140 \pm 0.2$ K for the surface magnetic order in 3D CrSBr offers potential explanations for the variation in the magnetic critical temperature of CrSBr. Finally, the temperature scale of $T^{**} = 155$ K was previously assigned to the onset of an intermediate *c*-axis incoherent ferromagnetic state, where the spins align ferromagnetically within individual *ab*-planes but randomly between adjacent *ab*-planes throughout the bulk of 3D CrSBr[21–24]. However, it is thermodynamically unlikely to achieve a phase transition from this intermediate order without *c*-axis coherence to the layered AFM order at $T_N = 132$ K for 3D bulk CrSBr, because the energy change scales with volume but the entropy change is proportional to the thickness, leading to a divergent (infinite) critical temperature for this phase transition. As a result, we revise the interpretation of $T^{**} = 155$ K to be a crossover temperature scale below which the spins form fluctuating, short-ranged patches both within and between *ab*-planes. Within individual patches, the spins on average align more along the *b*-axis, making the *b*-axis more different from the *a*-axis and thus resulting in the EQ SHG change across $T^{**}$ (see Supplementary Note 11 for detailed explanations).

### First-principle calculations explaining surface and extraordinary phase transitions

To understand the increase in the surface magnetism onset temperature in CrSBr despite the stronger fluctuation expected at the surface, we refer to the formula[44–47]:

$$T_N \approx \frac{T_{CW}}{A + \log(J_{||}/J')}. \quad (1)$$

Here, $T_{CW}$ denotes the mean-field Curie–Weiss temperature for monolayer CrSBr; $A$ is a constant of the order of 3–5; $J_{||}$ is the average characteristic intralayer exchange coupling; $J'$ represents a properly-defined combination of the interlayer coupling $J_\perp$ and the intralayer Ising anisotropy $D$, which arises from both the single site anisotropy and the Ising exchange –in a previous study[48], $J'$ was estimated as $J' = D + J_\perp + \sqrt{(D+J_\perp)^2 - D^2}$. Note that it is the small but nonzero intralayer anisotropy $D$ that maintains $T_N$ finite for monolayer CrSBr[21,24]. Within the mean-field theory, $T_{CW}$ is directly related to the intralayer exchange coupling strengths:

$$T_{CW} = -\frac{1}{3}S(S+1)(2J_1 + 4J_2 + 2J_3 + 4J_4 + 4J_5 + 2J_6 + 4J_7) \quad (2)$$

where $S = 3/2$ and $J_{1-7}$ are the intralayer exchange couplings up to the 7th nearest neighbor. From Eq. (1) and Eq. (2), we can see that the change in intralayer exchange coupling ($J_{1\text{-}7}$) will impact $T_N$ on a linear scale whereas the change in the intralayer anisotropy and interlayer coupling (included in $J'$) will influence $T_N$ on a logarithmical scale. Thus, the leading order contribution to the enhanced $T_N$ at the surface should be the change in the intralayer exchange coupling from bulk to surface.

To this effect, we performed first-principle density function theory (DFT) calculations to compute $T_{CW}$ based on the calculated $J_{1-7}$ from an isotropic Heisenberg spin Hamiltonian (Methods), and under four structural configurations (S1–4, discussed below). We have chosen an isotropic Heisenberg spin Hamiltonian for our DFT calculations, because the biaxial anisotropy of CrSBr has been shown to be at least 2–3 orders of magnitudes smaller than the intralayer exchange coupling, both through first-principle calculations[49,50] and experiments[23,51], and should have minor effects on $T_{CW}$ and $T_N$. The four strongest intralayer exchange couplings are found to be $J_1$, $J_2$, and $J_3$ that are FM, and $J_6$ that is AFM, as marked in Fig. 6a, whereas the

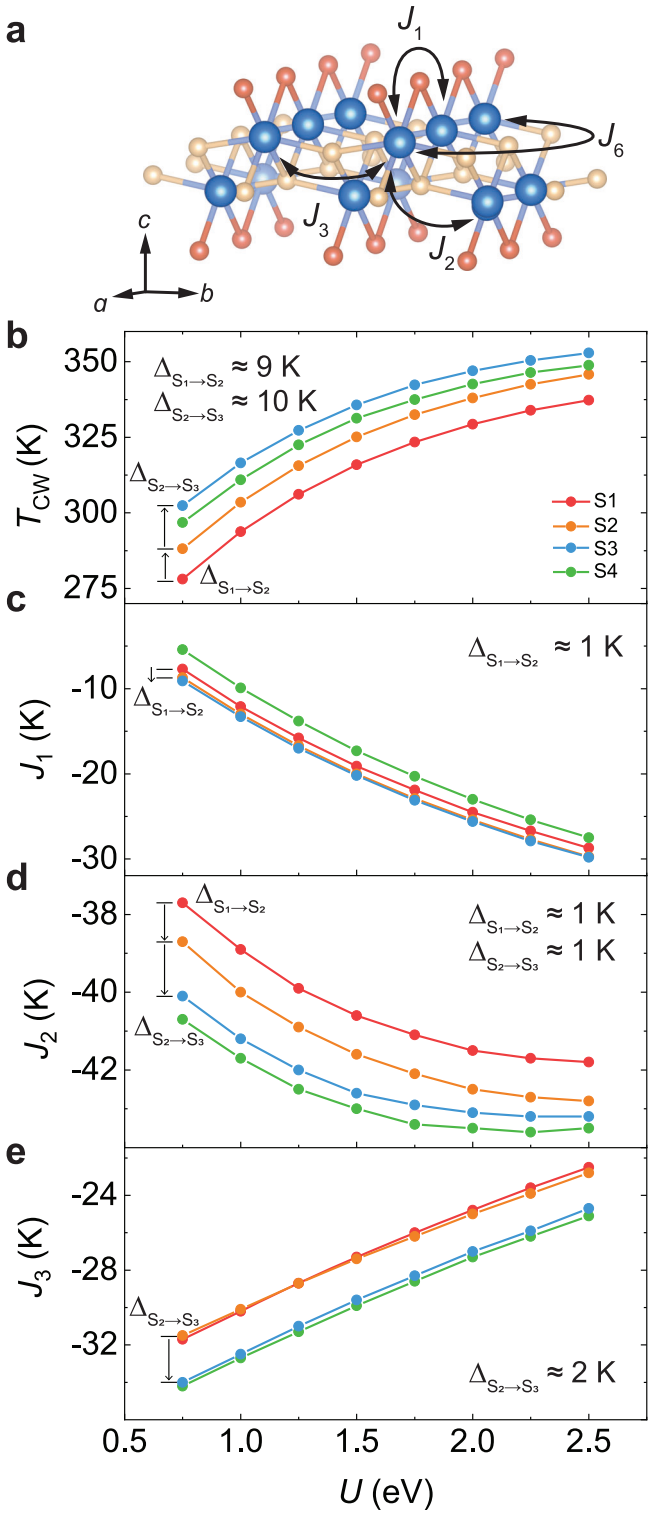


**Fig. 6 | DFT calculations explaining the origin of a higher transition temperature at the surface. a** exchange pathways for $J_1$, $J_2$, $J_3$ and $J_6$, overlaid on the CrSBr crystal structure. *U*-dependence of **b**, $T_{CW}$ **c**, $J_1$ **d**, $J_2$, and **e**, $J_3$ for S1: bulk CrSBr (red), S2: rigid monolayer (orange), S3: fixed *ab* monolayer (blue) and S4: free monolayer (green). $\Delta_{S1\to S2}$: change in $T_{CW}$ and corresponding $J$ from bulk to rigid monolayer. $\Delta_{S2\to S3}$: change in $T_{CW}$ and corresponding $J$ from rigid monolayer to fixed *ab* monolayer.

remaining $J_4$, $J_5$, and $J_7$ are negligibly small (see Supplementary Note 12). The four considered structures include bulk CrSBr (S1), rigid monolayer CrSBr that retains the atomic structure within the layer from the bulk (S2), fixed *ab* monolayer CrSBr that is derived from the intra-unit cell lattice relaxation while keeping the lattice constant same as the bulk (S3), and free monolayer CrSBr after the full lattice relaxation (S4). We vary the Hubbard $U$ across a wide range to verify the consistent and robust trend of $T_{CW}$ for the four scenarios: $T_{CW}$ increases from the bulk to the rigid monolayer, further enhances in the fixed *ab* monolayer, but decreases a bit in the free monolayer, as shown in Fig. 6b. This observed trend suggests two important factors that lead to the increase of $T_{CW}$: first, the absence of neighboring layers, and second, the intra-unit cell lattice relaxation. Following Eq. (1), both factors will contribute to the enhanced $T_N$ at the surface of CrSBr.

A close look into the evolution of the intralayer exchange coupling ($J_{1-7}$) across the four structures (S1–4) provides further insights into the two identified factors for the enhanced $T_{CW}$. The calculated $J_{1-3}$ show noticeable variations for S1 – 4, for a wide range of $U$, as shown in Fig. 6c–e, whereas $J_{4-7}$ remain unchanged across S1 – 4 structures (see Supplementary Note 12). For the first factor, the absence of neighboring layers leads to a substantial increase in both $J_1$ and $J_2$, i.e., $\Delta_{S1\rightarrow S2} = \sim 1$K shown in Fig. 6c, d. This increase in FM $J_1$ and $J_2$ by simply removing the neighboring layers is likely due to the suppression of a hopping path between the in-plane nearest ($J_1$) and second nearest ($J_2$) neighboring Cr sites going through neighboring layers that contributes an AFM intralayer exchange coupling to $J_1$ and $J_2$. For the second factor, the intra-unit cell lattice relaxation results in an increase in $J_2$ and $J_3$ by about 1 K and 2 K, respectively, i.e., $\Delta_{S2\rightarrow S3} = \sim 1$ K and $\sim 2$ K shown in Fig. 6d, e. The enhancement in $J_2$ is likely to arise from the increase of Cr-S-Cr angle between the two Cr sites within the unit cell (i.e., between the second nearest neighboring Cr sites), whereas the increase for $J_3$ mainly originates from the decrease of the Cr-S-Cr angle along the *b* axis (i.e., between the third nearest neighboring Cr sites). The strong dependence of the intralayer exchange coupling on the lattice structure has also been seen in strain-engineered CrSBr[52–54]. We further comment that while our calculations successfully explain the enhanced $T_N$ at the surface of 3D CrSBr, they are not intended to, and also cannot, provide the precise values of $T_N$ at the surface and inside the bulk of 3D CrSBr to match the experimental ones.

To summarize, we have successfully demonstrated the presence of surface and extraordinary phase transitions in a vdW AFM, bulk CrSBr, using the combination of bulk single-crystal EQ SHG and surface ED SHG. A clear temperature separation of 8 K is detected between the surface magnetism onset temperature, $T_S = 140 \pm 0.2$ K, and the bulk Néel temperature, $T_N = 132$ K, showing a counter-intuitive enhancement of the critical temperature at the surface. DFT calculations suggest two key factors for the increase of magnetic critical temperature at the CrSBr surface, namely, the absence of neighboring layer and the intra-unit cell lattice relaxation. Our results suggest multiple future research opportunities in vdW and 2D magnetism research. First, vdW magnets are a viable platform for realizing the parameter regime required for split surface and extraordinary phase transitions. In addition to CrSBr, immediate candidates include chromium chalcogenide halides[55,56] and chromium oxyhalides[57] that have similar magnetic properties to CrSBr, and $VI_3$[58], which exhibits a similar thickness dependence of critical temperature; namely, the onset temperature is higher in the few-layer samples than in the bulk. Second, static strain[52–54,59] and dynamic nonlinear phononics[60,61] are promising ways to tune the magnetism or enhance the magnetic critical temperature of CrSBr, thanks to its extreme sensitivity of intralayer exchange coupling to the intra-unit cell atomic arrangement. It is quite likely that a large pool of vdW magnets exhibit a similar exchange coupling dependence on lattice structure as CrSBr and therefore can be candidates for strain and light engineering of magnetism. Third, moiré superlattice of CrSBr can be fundamentally distinct from that of $CrI_3$[62–66] and offer a new platform for exploring moiré magnetism. On the one hand, the intralayer exchange coupling in CrSBr is shown in this work to significantly depend on the presence of the neighboring layers, which can lead to periodical modulations of intralayer exchange coupling in twisted CrSBr superlattices. This is in contrast to twisted $CrI_3$ superlattices where only modulations in interlayer exchange coupling are considered. On the other hand, CrSBr has an orthorhombic crystal lattice with one-dimensional electronic properties[67,68]. This highly anisotropic electronic property is in sharp contrast to the nearly isotropic electronic structure in $CrI_3$, and can offer unique moiré electronic and magnetic properties in twisted CrSBr.

## Methods

### Crystal growth and sample preparations

CrSBr single crystal is naturally grown using direct solid-vapor method through a box furnace. Cr powder (Alfa Aesar, 99.97%) and S powder (Alfa Aesar,99.5%) are accurately weighted inside the Ar-glovebox with total oxygen and moisture level less than 1 ppm. To facilitate the loading of bromide, the bromide liquid (99.8%) is initially solidified with the assist of liquid nitrogen. Cr powders, S powders and solid $Br_2$ are loaded into a clean quartz ampoule with the mole ratio of 1: 1.1: 1.2. Subsequently, the ampoule was sealed under vacuum using liquid nitrogen trap. We found out the extra amount of the S and Br created positive vapor pressure which effectively reduces the defects in the grown crystals and meanwhile promotes the larger size growth of single crystals. The quartz ampoule was heated up to 930 °C very slowly, stayed at this temperature for 20 h and followed by slowly cooling down to 750 °C (1°/h). The assembly is then quenched down to room temperature. Large size CrSBr will grow naturally at the bottom of the ampoule. A small amount of $CrBr_3$ is also found at the top of the quartz ampoule and can be easily separated from the CrSBr crystals. The thickness of the sample for SHG RA is about 0.2 mm. The thickness of the samples for the heat capacity and magnetization measurements is between 0.2 mm and 0.5 mm. The thickness of the samples for the TEM measurements is about ten layers for the in-plane measurement and a few nm for the cross-sectional measurement.

### Scanning transmission electron microscopy (STEM)

Plan-view specimens were prepared by exfoliating bulk CrSBr flakes on to polydimethylsiloxane (PDMS) gel stamps, which was transferred onto Norcada SiN TEM window grids with 2 μm holes. Cross-sectional specimens were prepared using the standard focus ion beam (FIB) lift-out method on Thermo Fisher Nova 200. HAADF-STEM was performed on JEOL 3100R05 (300 keV, 22 mrad) and Thermo Fisher Spectra 300 (300 keV, 21.4mrad) for plan-view and cross-section-view.

### Second harmonic generation

The incident ultrafast light source was of 50 fs pulse duration and 200 kHz repetition rate with a center wavelength 800 nm. It was focused down to a 15 μm diameter spot on the sample with an oblique incidence angle $\theta = 11.2°$ and a power of 850 μW. The polarizations of the incident and reflected light could be selected to be either parallel or perpendicular to each other, with the azimuthal angle $\phi$ changing correspondingly. The intensity of the reflected SHG signal with 400 nm wavelength was detected by a charge-coupled device (CCD). The temperature dependent SHG was performed during the warming up cycle with a heating rate 0.5 K/min. Additional wait time of 5 min ensures the stability of the temperature. The SHG RA data has been taken at a temperature with a temperature stability of 0.005 K.

### Extraction of temperature dependent $C^{ED}$ and $D^{EQ}$

the electric field in the $S_{in}$-$S_{out}$ channel from the surface magnetic ED SHG under $m'm2'$ is simulated to be

$$E^{\mathrm{SS,surface\ ED}}(\phi) = \left(\chi_{xyy} + 2\chi_{yxy}\right)\mathrm{Cos}[\phi]^2\mathrm{Sin}[\phi] + \chi_{xxx}\mathrm{Sin}[\phi]^3. \quad (3)$$

That from bulk EQ SHG under $mmm$ or $mmm1'$ is

$$\begin{aligned} E^{\mathrm{SS,bulk\ EQ}}(\phi) = & -\mathrm{Sin}[\theta](\chi_{xyxy} + 2\chi_{yyxx} - \chi_{yyyy})\mathrm{Cos}[\phi]^3\mathrm{Sin}[\phi] \\ & + (\chi_{xxxx} - 2\chi_{xxyy} - \chi_{yxyx})\mathrm{Cos}[\phi]\mathrm{Sin}[\phi]^3). \end{aligned} \quad (4)$$

We then constructed the functional form of the interfered SHG intensity through

$$\begin{aligned} I^{SS}(\phi) &= \left(E^{\mathrm{SS,surface\ ED}} + E^{\mathrm{SS,bulk\ EQ}}\right)^2 \\ &= ((\chi_{xyy} + 2\chi_{yxy})\mathrm{Cos}[\phi]^2\mathrm{Sin}[\phi] \\ &\quad + \chi_{xxx}\mathrm{Sin}[\phi]^3 - \mathrm{Sin}[\theta]((\chi_{xyxy} \\ &\quad + 2\chi_{yyxx} - \chi_{yyyy})\mathrm{Cos}[\phi]^3\mathrm{Sin}[\phi] \\ &\quad + (\chi_{xxxx} - 2\chi_{xxyy} - \chi_{yxyx})\mathrm{Cos}[\phi]\mathrm{Sin}[\phi]^3))^2. \end{aligned} \quad (5)$$

Through the fitting, four coefficients can be extracted: $C_1^{ED} = \chi_{xyy}^{ED} + 2\chi_{yxy}^{ED}$ and $C_2^{ED} = \chi_{xxx}^{ED}$ from the ED contribution, $D_1^{EQ} = \chi_{xyxy}^{EQ} + 2\chi_{yyxx}^{EQ} - \chi_{yyyy}^{EQ}$ and $D_2^{EQ} = \chi_{xxxx}^{EQ} - 2\chi_{xxyy}^{EQ} - \chi_{yxyx}^{EQ}$ from the EQ contribution. Consequently, our fitting can separate out the ED and EQ, and thus, surface and bulk unambiguously.

### First-principle calculations

The structure relaxation of CrSBr bulk and monolayers was performed using the Vienna ab initio simulation package (VASP)[69–71]. The projector augmented wave (PAW) potentials with the generalized gradient approximation (GGA) exchange-correlation potential in the Perdew-Burke-Ernzerhof variant (PBE)[72] were used. For the bulk relaxation, we use a Γ-centered $6 \times 6 \times 4\,k$ mesh, for monolayers a $7 \times 7 \times 1\,k$ mesh and an energy cutoff of 900 eV. The convergence criterion is that all forces are smaller than 3 mV/Å. Then, we performed all electron density functional theory calculations using the full potential local orbital (FPLO) code[73]. We used the non-local optB88-vdW functional to correct for dispersive interactions[74,75]. Energy mapping: We use DFT energy mapping[76,77] to determine the Heisenberg Hamiltonian parameters. For this purpose, we use a specially prepared 8-fold supercell of CrSBr with 16 symmetry inequivalent Cr sites. This allows us to determine the first seven in-plane exchange interactions $J_1$ to $J_7$. We use the GGA + $U$ exchange correlation functional with fully-localized limit double counting scheme, for eight different values of $U$ and $J_H = 0.72$ eV fixed following ref. 78. They were then fitted to the Heisenberg Hamiltonian of the form

$$H = \sum_{i<j} J_{ij}\boldsymbol{S}_i \cdot \boldsymbol{S}_j \quad (6)$$

with $Cr^{3+}$ spin operators $\boldsymbol{S}_i$, $|\boldsymbol{S}_i| = 3/2$. The Curie-Weiss temperature for this Hamiltonian is given by Eq. (2). Figure 6a was generated using VESTA software[79].

## Data availability

All data that support the finding of this work are included as main text and Supplementary Figs. Raw data and other data of this study are available from the corresponding author upon request. Source data are provided with this paper.

## References


1. Binder, K. & Hohenberg, P. C. Surface effects on magnetic phase-transitions. *Phys. Rev. B* **9**, 2194–2214 (1974).
2. Kumar, P. Magnetic phase transition at a surface: mean-field theory. *Phys. Rev. B* **10**, 2928–2933 (1974).
3. Lubensky, T. C. & Rubin, M. H. Critical phenomena in semi-infinite systems. II. Mean-field theory. *Phys. Rev. B* **12**, 3885–3901 (1975).
4. Bray, A. J. & Moore, M. A. Critical behavior of semi-infinite systems. *J. Phys. A Math. Gen.* **10**, 1927–1962 (1977).
5. Shen, Y. R. Surface second harmonic generation: a new technique for surface studies. *Annu. Rev. Mater. Sci.* **16**, 69–86 (1986).
6. Corn, R. M. & Higgins, D. A. Optical second harmonic generation as a probe of surface chemistry. *Chem. Rev.* **94**, 107–125 (1994).
7. Kirilyuk, A. & Rasing, T. Magnetization-induced-second-harmonic generation from surfaces and interfaces. *J. Opt. Soc. Am. B* **22**, 148–167 (2005).
8. Heinz, T. F., Tom, H. W. K. & Shen, Y. R. Determination of molecular orientation of monolayer adsorbates by optical second-harmonic generation. *Phys. Rev. A* **28**, 1883–1885 (1983).
9. Reif, J., Zink, J. C., Schneider, C.-M. & Kirschner, J. Effects of surface magnetism on optical second harmonic generation. *Phys. Rev. Lett.* **67**, 2878–2881 (1991).
10. Zhao, L. et al. A global inversion-symmetry-broken phase inside the pseudogap region of $YBa_2Cu_3O_y$. *Nat. Phys.* **13**, 250–254 (2017).
11. Torchinsky, D. H. et al. Structural distortion-induced magnetoelastic locking in $Sr_2IrO_4$ revealed through nonlinear optical harmonic generation. *Phys. Rev. Lett.* **114**, 096404 (2015).
12. Fiebig, M., Pavlov, V. V. & Pisarev, R. V. Second-harmonic generation as a tool for studying electronic and magnetic structures of crystals: review. *J. Opt. Soc. Am. B* **22**, 96–118 (2005).
13. Zhao, L. et al. Evidence of an odd-parity hidden order in a spin-orbit coupled correlated iridate. *Nat. Phys.* **12**, 32–36 (2016).
14. Yokota, H., Hayashida, T., Kitahara, D. & Kimura, T. Three-dimensional imaging of ferroaxial domains using circularly polarized second harmonic generation microscopy. *npj Quantum Mater.* **7**, 106 (2022).
15. Owen, R. et al. Second-order nonlinear optical and linear ultraviolet-visible absorption properties of the type-II multiferroic candidates $RbFe(AO_4)_2$ (A = Mo, Se, S). *Phys. Rev. B* **103**, 054104 (2021).
16. de la Torre, A. et al. Mirror symmetry breaking in a model insulating cuprate. *Nat. Phys.* **17**, 777–781 (2021).
17. Luo, X. et al. Ultrafast modulations and detection of a ferro-rotational charge density wave using time-resolved electric quadrupole second harmonic generation. *Phys. Rev. Lett.* **127**, 126401 (2021).
18. Jin, W. et al. Observation of a ferro-rotational order coupled with second-order nonlinear optical fields. *Nat. Phys.* **16**, 42–46 (2020).
19. Guo, X. et al. Ferrorotational domain walls revealed by electric quadrupole second harmonic generation microscopy. *Phys. Rev. B* **107**, L180102 (2023).
20. Telford, E. J. et al. Layered antiferromagnetism induces large negative magnetoresistance in the van der Waals semiconductor CrSBr. *Adv. Mater.* **32**, 2003240 (2020).
21. Lee, K. et al. Magnetic order and symmetry in the 2D semiconductor CrSBr. *Nano Lett.* **21**, 3511–3517 (2021).
22. Liu, W. et al. A three-stage magnetic phase transition revealed in ultrahigh-quality van der Waals bulk magnet CrSBr. *ACS Nano* **16**, 15917–15926 (2022).
23. Scheie, A. et al. Spin waves and magnetic exchange Hamiltonian in CrSBr. *Adv. Sci.* **9**, 2202467 (2022).
24. Telford, E. J. et al. Coupling between magnetic order and charge transport in a two-dimensional magnetic semiconductor. *Nat. Mater.* **21**, 754–760 (2022).

25. Ye, C. et al. Layer-dependent interlayer antiferromagnetic spin reorientation in air-stable semiconductor CrSBr. *ACS Nano* **16**, 11876–11883 (2022).
26. Lopez-Paz, S. A. et al. Dynamic magnetic crossover at the origin of the hidden-order in van der Waals antiferromagnet CrSBr. *Nat. Commun.* **13**, 4745 (2022).
27. Goser, O., Paul, W. & Kahle, H. G. Magnetic properties of CrSBr. *J. Magn. Magn. Mater.* **92**, 129–136 (1990).
28. Klein, J. et al. Sensing the local magnetic environment through optically active defects in a layered magnetic semiconductor. *ACS Nano* **17**, 288–299 (2023).
29. Huang, B. et al. Layer-dependent ferromagnetism in a van der Waals crystal down to the monolayer limit. *Nature* **546**, 270–273 (2017).
30. Sun, Z. et al. Giant nonreciprocal second-harmonic generation from antiferromagnetic bilayer $CrI_3$. *Nature* **572**, 497–501 (2019).
31. Gong, C. et al. Discovery of intrinsic ferromagnetism in two-dimensional van der Waals crystals. *Nature* **546**, 265–269 (2017).
32. Deng, Y. et al. Gate-tunable room-temperature ferromagnetism in two-dimensional $Fe_3GeTe_2$. *Nature* **563**, 94–99 (2018).
33. Kim, K. et al. Suppression of magnetic ordering in XXZ-type antiferromagnetic monolayer $NiPS_3$. *Nat. Commun.* **10**, 345 (2019).
34. Wang, X. et al. Raman spectroscopy of atomically thin two-dimensional magnetic iron phosphorus trisulfide ($FePS_3$) crystals. *2D Mater.* **3**, 031009 (2016).
35. Lee, J.-U. et al. Ising-type magnetic ordering in atomically thin $FePS_3$. *Nano Lett.* **16**, 7433–7438 (2016).
36. Liu, P. et al. Exploring the magnetic ordering in atomically thin antiferromagnetic $MnPSe_3$ by Raman spectroscopy. *J. Alloy. Compd.* **828**, 154432 (2020).
37. Ju, H. et al. Influence of stacking disorder on cross-plane thermal transport properties in $TMPS_3$ (*TM* = Mn, Ni, Fe). *Appl. Phys. Lett.* **117**, 063103 (2020).
38. Mortelmans, W., De Gendt, S., Heyns, M. & Merckling, C. Epitaxy of 2D chalcogenides: aspects and consequences of weak van der Waals coupling. *Appl. Mater. Today* **22**, 100975 (2021).
39. Zhao, X. et al. Healing of planar defects in 2D materials via grain boundary sliding. *Adv. Mater.* **31**, 1900237 (2019).
40. Rooney, A. P. et al. Anomalous twin boundaries in two dimensional materials. *Nat. Commun.* **9**, 3597 (2018).
41. Fiebig, M., Frohlich, D., Sluyterman, G. & Pisarev, R. V. Domain topography of antiferromagnetic $Cr_2O_3$ by second-harmonic generation. *Appl. Phys. Lett.* **66**, 2906–2908 (1995).
42. Fiebig, M., Frohlich, D., Krichevtsov, B. B. & Pisarev, R. V. Second harmonic generation and magnetic-dipole-electric-dipole interference in antiferromagnetic $Cr_2O_3$. *Phys. Rev. Lett.* **73**, 2127–2130 (1994).
43. Diehl, H. W. & Dietrich, S. Field-theoretical approach to static critical phenomena in semi-infinite systems. *Z. Phys. B* **42**, 65–86 (1981).
44. Chakravarty, S., Halperin, B. I. & Nelson, D. R. Low-temperature behavior of two-dimensional quantum antiferromagnets. *Phys. Rev. Lett.* **60**, 1057–1060 (1988).
45. Liu, S. H. Critical temperature of pseudo-one- and -two-dimensional magnetic systems. *J. Magn. Magn. Mater.* **82**, 294–296 (1989).
46. Wei, G. Z. & Du, A. Magnetic properties of layered Heisenberg antiferromagnets. *Phys. Status Solidi (b)* **175**, 237–245 (1993).
47. Yasuda, C. et al. Neel temperature of quasi-low-dimensional Heisenberg antiferromagnets. *Phys. Rev. Lett.* **94**, 217201 (2005).
48. Irkhin, V. Y. & Katanin, A. A. Thermodynamics of isotropic and anisotropic layered magnets: renormalization-group approach and 1/N expansion. *Phys. Rev. B* **57**, 379–391 (1998).
49. Wang, H., Qi, J., Qian, X. Electrically tunable high Curie temperature two-dimensional ferromagnetism in van der Waals layered crystals. *Appl. Phys. Lett.* **117**, 083102 (2020).
50. Bo, X., Li, F., Xu, X., Wan, X. & Pu, Y. Calculated magnetic exchange interactions in the van der Waals layered magnet CrSBr. *New J. Phys.* **25**, 013026 (2023).
51. Bae, Y. J. et al. Exciton-coupled coherent magnons in a 2D semiconductor. *Nature* **609**, 282–286 (2022).
52. Esteras, D. L., Rybakov, A., Ruiz, A. M. & Baldovi, J. J. Magnon straintronics in the 2D van der Waals ferromagnet CrSBr from first-principles. *Nano Lett.* **22**, 8771–8778 (2022).
53. Yang, K., Wang, G., Liu, L., Lu, D. & Wu, H. Triaxial magnetic anisotropy in the two-dimensional ferromagnetic semiconductor CrSBr. *Phys. Rev. B* **104**, 144416 (2021).
54. Diao, Y. et al. Strain-regulated magnetic phase transition and perpendicular magnetic anisotropy in CrSBr monolayer. *Phys. E Low Dimens. Syst. Nanostruct.* **147**, 115590 (2023).
55. Hou, Y., Xue, F., Qiu, L., Wang, Z. & Wu, R. Multifunctional two-dimensional van der Waals Janus magnet Cr-based dichalcogenide halides. *npj Comput. Mater.* **8**, 120 (2022).
56. Han, R., Jiang, Z. & Yan, Y. Prediction of novel 2D intrinsic ferromagnetic materials with high Curie temperature and large perpendicular magnetic anisotropy. *J. Phys. Chem. C* **124**, 7956–7964 (2020).
57. Miao, N., Xu, B., Zhu, L., Zhou, J. & Sun, Z. 2D intrinsic ferromagnets from van der Waals antiferromagnets. *J. Am. Chem. Soc.* **140**, 2417–2420 (2018).
58. Lin, Z. et al. Magnetism and its structural coupling effects in 2D Ising ferromagnetic insulator $VI_3$. *Nano Lett.* **21**, 9180–9186 (2021).
59. Cenker, J. et al. Reversible strain-induced magnetic phase transition in a van der Waals magnet. *Nat. Nanotechnol.* **17**, 256–261 (2022).
60. Disa, A. S. et al. Photo-induced high-temperature ferromagnetism in $YTiO_3$. *Nature* **617**, 73–78 (2023).
61. Disa, A. S., Nova, T. F. & Cavalleri, A. Engineering crystal structures with light. *Nat. Phys.* **17**, 1087–1092 (2021).
62. Cheng, G. et al. Electrically tunable moiré magnetism in twisted double bilayers of chromium triiodide. *Nat. Electron.* **6**, 434–442 (2023).
63. Xu, Y. et al. Coexisting ferromagnetic-antiferromagnetic state in twisted bilayer $CrI_3$. *Nat. Nanotechnol.* **17**, 143–147 (2022).
64. Song, T. et al. Direct visualization of magnetic domains and moire magnetism in twisted 2D magnets. *Science* **374**, 1140–1144 (2021).
65. Xie, H. et al. Evidence of non-collinear spin texture in magnetic moire superlattices. *Nat. Phys.* **19**, 1150–1155 (2023).
66. Xie, H. et al. Twist engineering of the two-dimensional magnetism in double bilayer chromium triiodide homostructures. *Nat. Phys.* **18**, 30–36 (2022).
67. Klein, J. et al. The bulk van der Waals layered magnet CrSBr is a quasi-1D material. *ACS Nano* **17**, 5316–5328 (2023).
68. Wu, F. et al. Quasi-1D electronic transport in a 2D magnetic semiconductor. *Adv. Mater.* **34**, 2109759 (2022).
69. Kresse, G. & Furthmuller, J. Efficiency of ab-initio total energy calculations for metals and semiconductors using a plane-wave basis set. *Comp. Mater. Sci.* **6**, 15–50 (1996).
70. Kresse, G. & Furthmuller, J. Efficient iterative schemes for ab initio total-energy calculations using a plane-wave basis set. *Phys. Rev. B* **54**, 11169–11186 (1996).
71. Kresse, G. & Hafner, J. Ab initio molecular-dynamics for liquid-metals. *Phys. Rev. B* **47**, 558–561 (1993).
72. Perdew, J. P., Burke, K. & Ernzerhof, M. Generalized gradient approximation made simple. *Phys. Rev. Lett.* **77**, 3865–3868 (1996).
73. Koepernik, K. & Eschrig, H. Full-potential nonorthogonal local-orbital minimum-basis band-structure scheme. *Phys. Rev. B* **59**, 1743–1757 (1999).
74. Klimes, J., Bowler, D. R., Michaelides, A. Van der Waals density functionals applied to solids. *Phys. Rev. B* **83**, 195131 (2011).

75. Klimes, J., Bowler, D. R. & Michaelides, A. Chemical accuracy for the van der Waals density functional. *J. Phys. Condens. Matter* **22**, 022201 (2010).
76. Chillal, S. et al. Evidence for a three-dimensional quantum spin liquid in $PbCuTe_2O_6$. *Nat. Commun.* **11**, 2348 (2020).
77. Ghosh, P. et al. Breathing chromium spinels: a showcase for a variety of pyrochlore Heisenberg Hamiltonians. *npj Quantum Mater.* **4**, 63 (2019).
78. Mizokawa, T. & Fujimori, A. Electronic structure and orbital ordering in perovskite-type 3d transition-metal oxides studied by Hartree-Fock band-structure calculations. *Phys. Rev. B* **54**, 5368–5380 (1996).
79. Momma, K. & Izumi, F. VESTA 3 for three-dimensional visualization of crystal, volumetric and morphology data. *J. Appl. Crystallogr.* **44**, 1272–1276 (2011).

## Acknowledgements

L.Z., H.D. and K.S. acknowledge the support by the Office of Navy Research grant no. N00014-21-1-2770 and the Gordon and Betty Moore Foundation grant no. N031710. L.Z. also acknowledges the support by AFOSR YIP grant no. FA9550-21-1-0065 and Alfred P. Sloan foundation. B.L. acknowledges the support by US Air Force Office of Scientific Research Grant No. FA9550-19-1-0037, National Science Foundation (NSF)- DMREF- 1921581 and Office of Naval Research (ONR) grant no. N00014-23-1-2020. R.H. acknowledges the financial support of the W.M. Keck Foundation. This work made use of the Michigan Center for Materials Characterization (MC2). I.I.M. was supported, at an early stage, by the U.S. Department of Energy through the grant No. DE-SC0021089, and later by the Office of Naval Research through the grant N00014-23-1-2480. M.S. acknowledges the support by JSPS KAKENHI grant No. 22H01181. L.L. acknowledges the support by the National Science Foundation under Award No. DMR-2317618 (electrical transport measurements) and the support by the Department of Energy under Award No. DE-SC0020184 (magnetization measurements).

## Author contributions

X.G. and L.Z. conceived the project. X.G. performed the SHG measurements and data analysis under the supervision of L.Z., H.D. and K.S. W.L., A.L.N.K. and B.L. provided the CrSBr single crystals. J.S., S.H.S. and R.H. performed the HAADF-STEM measurements. W.L., D.Z., L.L. and B.L. performed the heat capacity and magnetization measurements. M.S., H.O.J. and I.I.M. performed and interpreted the DFT calculations. X.G. and L.Z. wrote the manuscript. All authors discussed the results.

## Competing interests

The authors declare no competing interests.

## Additional information

**Supplementary information** The online version contains supplementary material available at https://doi.org/10.1038/s41467-024-50900-1.

**Correspondence** and requests for materials should be addressed to Bing Lv or Liuyan Zhao.

**Peer review information** *Nature Communications* thanks the anonymous reviewers for their contribution to the peer review of this work. A peer review file is available.

# Supplementary Information

## Extraordinary Phase Transition Revealed in a van der Waals Antiferromagnet

Xiaoyu Guo[1, Δ] , Wenhao Liu[2, Δ], Jonathan Schwartz[3], Suk Hyun Sung[3], Dechen Zhang[1], Makoto Shimizu[4,*], Aswin L. N. Kondusamy[2], Lu Li[1], Kai Sun[1], Hui Deng[1], Harald O. Jeschke[5], Igor I. Mazin[6], Robert Hovden[3], Bing Lv[2, +] and Liuyan Zhao[1, +]

[1] *Department of Physics, University of Michigan, Ann Arbor, MI 48019, USA*

[2] *Department of Physics, the University of Texas at Dallas, Richardson, TX 75080, USA*

[3] *Department of Materials Science and Engineering, University of Michigan, Ann Arbor, MI 48109, USA*

[4] *Department of Physics, Okayama University, Okayama 700-8530, Japan*

[5] *Research Institute for Interdisciplinary Science, Okayama University, Okayama 700-8530, Japan*

[6] *Department of Physics and Astronomy, and Quantum Science and Engineering Center, George Mason University, Fairfax, VA 22030, USA*

[+] Corresponding to: blv@utdallas.edu, lyzhao@umich.edu

[*] Present address: *Department of Physics, Graduate School of Science, Kyoto University, Kyoto 606-8502, Japan*

[Δ] Authors contribute equally

**Supplementary Note 1: extensive scanning transmission electron microscopy (STEM) characterization**

We checked the robustness of both the stacking sequence and the atomic lattice for CrSBr using scanning transmission electron microscopy (STEM). The wide-range in-plane atomic resolution STEM images rarely show atomic defects (Supplementary Fig. 1a) and the wide-range cross-sectional STEM images consistently show the right overlying stacking between layers (Supplementary Fig. 1b). Therefore, we believe that the crystal structure of CrSBr is robust and that our sample is of high quality.

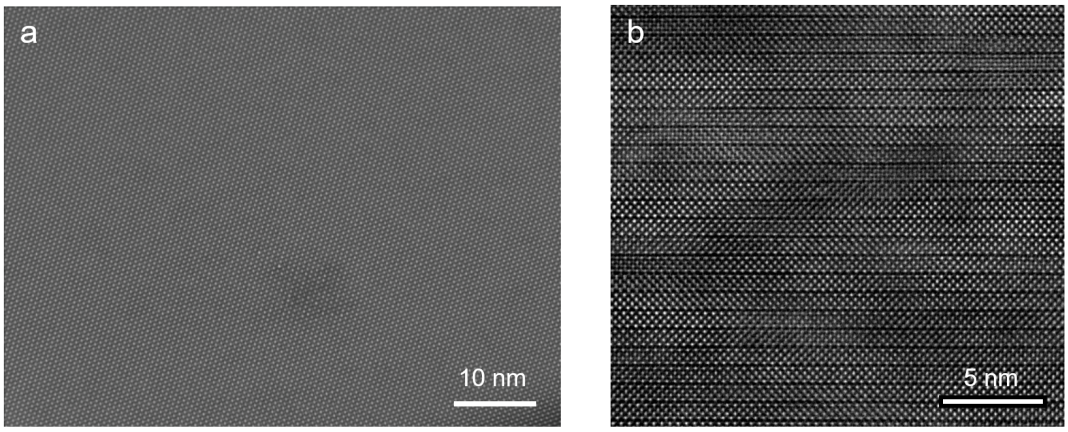


**Supplementary Fig. 1 | Extensive STEM characterizations. a**. wide-range atomic resolution scanning transmission electron microscopy (STEM) image of CrSBr in the *ab*-plane. **b** Side-view atomic resolution STEM image in the *ac*-plane.

**Supplementary Note 2: atomic force microscopy (AFM) characterization**

Atomic force microscopy (AFM) captures the surface roughness and atomic steps, with a height resolution of ~ 0.1 nm. Supplementary Fig. 2a shows a representative AFM image taken over a CrSBr sample where we performed second harmonic generation rotational anisotropy (SHG RA) measurements. Over an area of about 130 x 250 $\mu m^2$, we only observed a few atomic step sizes of height ~1-2 nm in the lower right corner of a 30 x 55 $\mu m^2$ area (see a linecut in Supplementary Fig. 2b). For the rest of the field of view, it is a single atomic terrace with a standard deviation of height to be 0.086 nm (see the histogram of height distribution in Supplementary Fig. 2c). Therefore, our CrSBr single crystals with freshly cleaved surfaces show highly flat surfaces with low density of atomic steps.

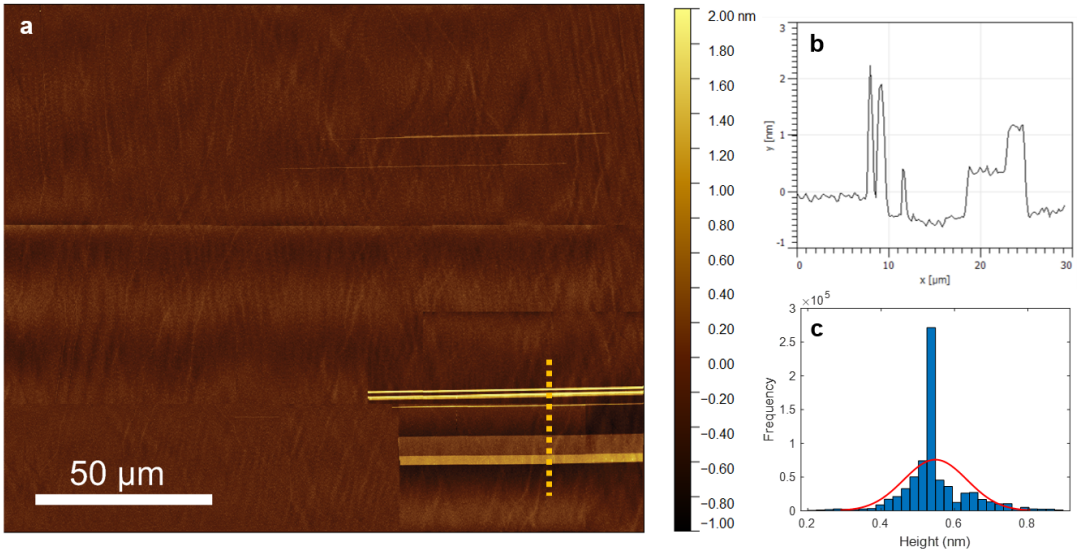


**Supplementary Fig. 2 | AFM characterization of CrSBr sample. a**. atomic force microscopy (AFM) image taken over a CrSBr sample. **b**. Linecut height profile indicated by the yellow dash line in **a**. **c**. Histogram of height distribution from the flat region. The red curve indicates the Gaussian fit, yielding the standard deviation to be 0.086 nm.

**Supplementary Note 3: magnetization measurement of bulk CrSBr**

We performed magnetization measurement on the same sample where the SHG RA measurements were performed. As is shown in Supplementary Fig. 3a, apart from the diverging behavior at $T_N$ that indicates the bulk antiferromagnetic (AFM) phase transition, an anomaly is evident at $T_F$ = 30 K, marking the onset of the possible ferromagnetic phase transition. Here, only a weak signature has been observed in our high-quality crystal, consistent with the proposal that this phase transition is related to the magnetic defects inside the crystal. We have also fitted the high temperature (>150 K) magnetic susceptibility using the Curie-Weiss Law:

$$\chi = \chi_0 + \frac{C}{T - T_0}, \tag{1}$$

where $\chi_0$ is the temperature-independent susceptibility arising from the background, $C$ is a constant and $T_0$ is the Curie-Weiss temperature (Supplementary Fig. 3b). The fitted $T_0$ = 152 K.

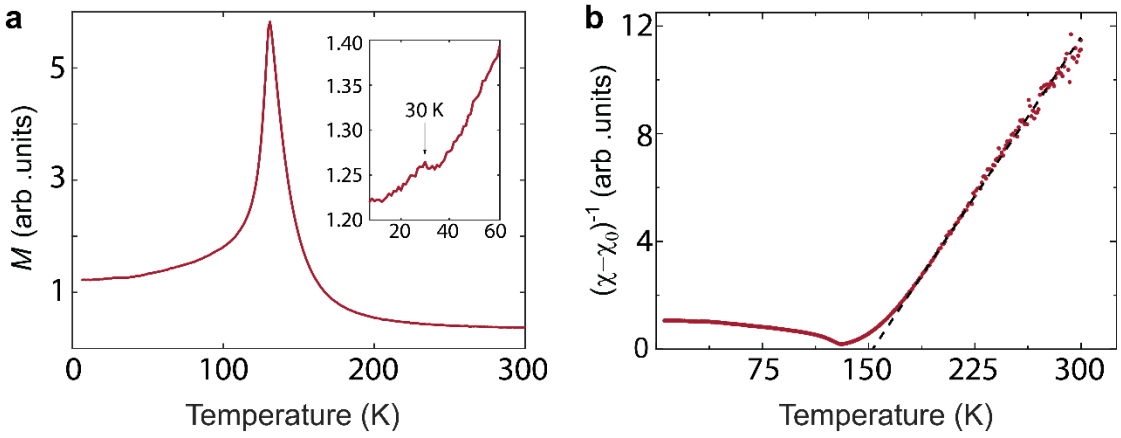


**Supplementary Fig. 3 | Magnetization measurement of bulk CrSBr. a**, Magnetization measured as a function of temperature. A magnetic field of 1000 Oe was applied along the crystallographic *b*-axis for the measurement. The inset shows the zoom-in region illustrating the anomaly at $T_F$ = 30 K, where the possible ferromagnetic phase transition happens. **b**, Temperature dependence of the inverse magnetic susceptibility. The black dash line shows the fitting of the data using the Curie−Weiss law.

**Supplementary Note 4: high temperature oblique SHG RA from bulk CrSBr and SHG radiation source determination**

Supplementary Fig. 4 shows the SHG RA patterns measured at 293 K and 185 K on the same sample but at different locations. Both sets of the patterns show the same symmetries: two-fold rotational symmetry about the *c*-axis ($C_{2c}$), and mirror symmetries with respect to mirrors perpendicular to *a*-axis ($m_a$) and *b*-axis ($m_b$), consistent with the crystallography point group *mmm*. They also show similar shapes and SHG intensities. The characteristic temperature scale $T^* = 185$ K that indicates the presence of spin-spin interaction cannot be captured by our SHG RA technique.

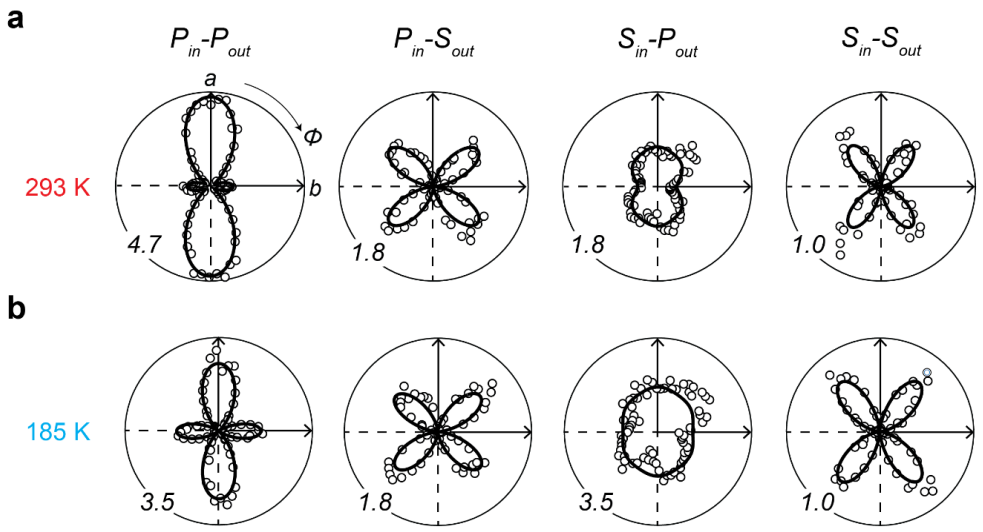


**Supplementary Fig. 4 | SHG RA patterns at high temperatures.** Four channels of SHG RA patterns measured at **a**, 293 K and **b**, 185 K. Experiment data (circles) are fitted by functional forms simulated based on group theory analysis (solid curves). Numbers at the corners indicate the scales of the polar plots, with 1.0 corresponding to 1 fW.

The experimental data has been fitted with the functional forms simulated from the electric quadrupole (EQ) contribution under the point group *mmm* and shown as solid curves in Supplementary Fig. 4. Other radiation sources including surface electric dipole (ED), bulk magnetic dipole (MD) and electric field induced second harmonic (EFISH) have been ruled out. Supplementary Fig. 5 shows the SHG RA raw data measured at $T = 185$ K, together with the simulated pattens under bulk EQ (point group *mmm*), surface ED (point group *mm2*), bulk MD (point group *mmm*), and EFISH at the surface, with the induced dipole along the *c*-axis (point

group *mmm*), using the functional forms provided. We see that the raw data match the EQ simulation the best. Specifically, in the other three cases, there is always one channel showing no SHG signal, in contrast with our raw data, where SHG signals are present in all four channels. Consequently, we have pinned down bulk EQ as the primary source for our SHG signal.

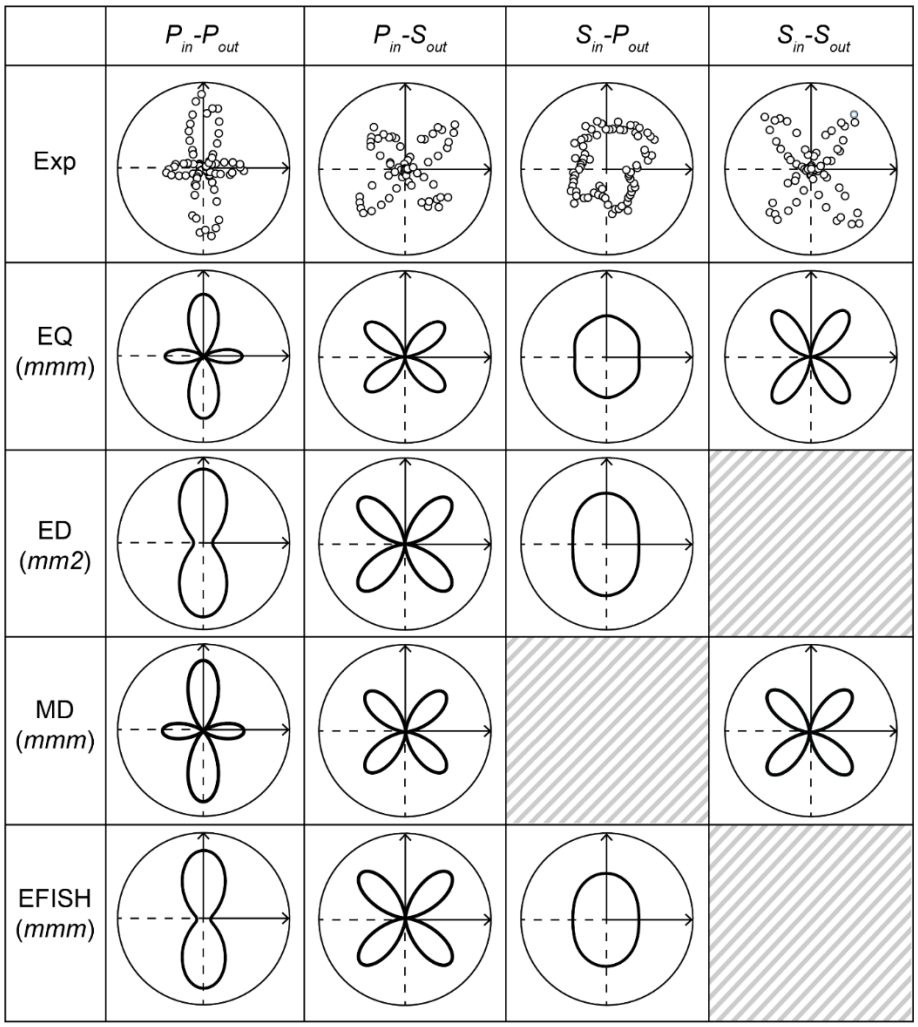


**Supplementary Fig. 5 | Simulation results for various SHG radiation sources.** SHG RA raw data measured at 185 K in all four channels, together with the simulated pattens from bulk electric quadrupole (EQ), surface electric dipole (ED), bulk magnetic dipole (MD) and electric-field-induced second harmonic (EFISH) at the surface.

Here, we provide the simulated functional forms of the SHG RA patterns at the high temperature from different radiation sources under the corresponding point groups that are used to construct Supplementary Fig. 5.

1. **Bulk EQ** under the point group ***mmm***:

The rank-4 nonlinear optical susceptibility tensor has the form:

$$\chi^{EQ}_{mmm} = \begin{pmatrix} \begin{pmatrix} \chi_{xxxx} & 0 & 0 \\ 0 & \chi_{xxyy} & 0 \\ 0 & 0 & \chi_{xxzz} \end{pmatrix} & \begin{pmatrix} 0 & \chi_{xyxy} & 0 \\ \chi_{xxyy} & 0 & 0 \\ 0 & 0 & 0 \end{pmatrix} & \begin{pmatrix} 0 & 0 & \chi_{xzxz} \\ 0 & 0 & 0 \\ \chi_{xxzz} & 0 & 0 \end{pmatrix} \\ \begin{pmatrix} 0 & \chi_{yyxx} & 0 \\ \chi_{yxyx} & 0 & 0 \\ 0 & 0 & 0 \end{pmatrix} & \begin{pmatrix} \chi_{yyxx} & 0 & 0 \\ 0 & \chi_{yyyy} & 0 \\ 0 & 0 & \chi_{yyzz} \end{pmatrix} & \begin{pmatrix} 0 & 0 & 0 \\ 0 & 0 & \chi_{yzyz} \\ 0 & \chi_{yyzz} & 0 \end{pmatrix} \\ \begin{pmatrix} 0 & 0 & \chi_{zzxx} \\ 0 & 0 & 0 \\ \chi_{zxzx} & 0 & 0 \end{pmatrix} & \begin{pmatrix} 0 & 0 & 0 \\ 0 & 0 & \chi_{zzyy} \\ 0 & \chi_{zyzy} & 0 \end{pmatrix} & \begin{pmatrix} \chi_{zzxx} & 0 & 0 \\ 0 & \chi_{zzyy} & 0 \\ 0 & 0 & \chi_{zzzz} \end{pmatrix} \end{pmatrix}, \tag{2}$$

leading to the following functional forms for the radiation.

In the $P_{in}$-$P_{out}$ channel:

$$\begin{aligned} S^{PP}_{EQ,mmm} = {} & \mathrm{Sin}[\theta]^2(-\chi_{zzzz}\mathrm{Cos}[\theta]\mathrm{Sin}[\theta]^2 - \mathrm{Cos}[\theta]^3(\chi_{zxzx}\mathrm{Cos}[\phi]^2 \\ & + \chi_{zyzy}\mathrm{Sin}[\phi]^2) + 2\mathrm{Cos}[\theta]\mathrm{Sin}[\theta]^2(\chi_{zzxx}\mathrm{Cos}[\phi]^2 \\ & + \chi_{zzyy}\mathrm{Sin}[\phi]^2))^2 \\ & + \mathrm{Cos}[\theta]^2(2\mathrm{Cos}[\theta]^2\mathrm{Sin}[\theta](\chi_{xxzz}\mathrm{Cos}[\phi]^2 + \chi_{yyzz}\mathrm{Sin}[\phi]^2) \\ & - \mathrm{Sin}[\theta]^3(\chi_{xzxz}\mathrm{Cos}[\phi]^2 + \chi_{yzyz}\mathrm{Sin}[\phi]^2) \\ & - \mathrm{Cos}[\theta]^2\mathrm{Sin}[\theta](\chi_{xxxx}\mathrm{Cos}[\phi]^4 + (2\chi_{xxyy} + \chi_{xyxy} + \chi_{yxyx} \\ & + 2\chi_{yyxx})\mathrm{Cos}[\phi]^2\mathrm{Sin}[\phi]^2 + \chi_{yyyy}\mathrm{Sin}[\phi]^4))^2. \end{aligned} \tag{3}$$

In the $P_{in}$-$S_{out}$ channel:

$$\begin{aligned} S^{PS}_{EQ,mmm} = {} & (2(\chi_{xxzz} - \chi_{yyzz})\mathrm{Cos}[\theta]^2\mathrm{Cos}[\phi]\mathrm{Sin}[\theta]\mathrm{Sin}[\phi] - (\chi_{xzxz} \\ & - \chi_{yzyz})\mathrm{Cos}[\phi]\mathrm{Sin}[\theta]^3\mathrm{Sin}[\phi] - \mathrm{Cos}[\theta]^2\mathrm{Sin}[\theta]((\chi_{xxxx} \\ & - \chi_{yxyx} - 2\chi_{yyxx})\mathrm{Cos}[\phi]^3\mathrm{Sin}[\phi] + (2\chi_{xxyy} + \chi_{xyxy} \\ & - \chi_{yyyy})\mathrm{Cos}[\phi]\mathrm{Sin}[\phi]^3))^2. \end{aligned} \tag{4}$$

In the $S_{in}$-$P_{out}$ channel:

$$S_{EQ,mmm}^{SP} = \mathrm{Cos}[\theta]^2\mathrm{Sin}[\theta]^2(\chi_{\mathrm{zyzy}}\mathrm{Cos}[\phi]^2 + \chi_{\mathrm{zxzx}}\mathrm{Sin}[\phi]^2)^2 + \mathrm{Cos}[\theta]^2\mathrm{Sin}[\theta]^2(\chi_{\mathrm{xyxy}}\mathrm{Cos}[\phi]^4 + (\chi_{\mathrm{xxxx}} - 2(\chi_{\mathrm{xxyy}} + \chi_{\mathrm{yyxx}}) + \chi_{\mathrm{yyyy}})\mathrm{Cos}[\phi]^2\mathrm{Sin}[\phi]^2 + \chi_{\mathrm{yxyx}}\mathrm{Sin}[\phi]^4)^2. \quad (5)$$

In the $S_{\mathrm{in}}$-$S_{\mathrm{out}}$ channel:

$$S_{EQ,mmm}^{SS} = \mathrm{Sin}[\theta]^2((\chi_{\mathrm{xyxy}} + 2\chi_{\mathrm{yyxx}} - \chi_{\mathrm{yyyy}})\mathrm{Cos}[\phi]^3\mathrm{Sin}[\phi] + (\chi_{\mathrm{xxxx}} - 2\chi_{\mathrm{xxyy}} - \chi_{\mathrm{yxyx}})\mathrm{Cos}[\phi]\mathrm{Sin}[\phi]^3)^2, \quad (6)$$

where $\theta$ is the incident polar angle and $\phi$ the azimuth angle between the scattering plane and the crystallographic *a*-axis.

2. **Surface ED** under the point group $\boldsymbol{mm2}$ and ***i*-type surface ED** under the magnetic point group $\boldsymbol{m'm2'}$:

The rank-3 nonlinear optical susceptibility tensor has the form:

$$\chi_{mm2}^{ED} = \begin{pmatrix} \begin{pmatrix} 0 \\ 0 \\ \chi_{\mathrm{xxz}} \end{pmatrix} & \begin{pmatrix} 0 \\ 0 \\ 0 \end{pmatrix} & \begin{pmatrix} \chi_{\mathrm{xxz}} \\ 0 \\ 0 \end{pmatrix} \\ \begin{pmatrix} 0 \\ 0 \\ 0 \end{pmatrix} & \begin{pmatrix} 0 \\ 0 \\ \chi_{\mathrm{yyz}} \end{pmatrix} & \begin{pmatrix} 0 \\ \chi_{\mathrm{yyz}} \\ 0 \end{pmatrix} \\ \begin{pmatrix} \chi_{\mathrm{zxx}} \\ 0 \\ 0 \end{pmatrix} & \begin{pmatrix} 0 \\ \chi_{\mathrm{zyy}} \\ 0 \end{pmatrix} & \begin{pmatrix} 0 \\ 0 \\ \chi_{\mathrm{zzz}} \end{pmatrix} \end{pmatrix}, \quad (7)$$

leading to the following functional forms for the radiation.

In the $P_{\mathrm{in}}$-$P_{\mathrm{out}}$ channel:

$$S_{ED,mm2}^{PP} = 4\mathrm{Cos}[\theta]^4\mathrm{Sin}[\theta]^2\left(\chi_{\mathrm{xxz}}\mathrm{Cos}[\phi]^2 + \chi_{\mathrm{yyz}}\mathrm{Sin}[\phi]^2\right)^2 + \mathrm{Sin}[\theta]^2\left(\chi_{\mathrm{zzz}}\mathrm{Sin}[\theta]^2 + \mathrm{Cos}[\theta]^2\left(\chi_{\mathrm{zxx}}\mathrm{Cos}[\phi]^2 + \chi_{\mathrm{zyy}}\mathrm{Sin}[\phi]^2\right)\right)^2. \quad (8)$$

In the $P_{\mathrm{in}}$-$S_{\mathrm{out}}$ channel:

$$S_{ED,mm2}^{PS} = 4\left(\chi_{xxz} - \chi_{yyz}\right)^2 \mathrm{Cos}[\theta]^2 \mathrm{Cos}[\phi]^2 \mathrm{Sin}[\theta]^2 \mathrm{Sin}[\phi]^2. \quad (9)$$

In the $S_{in}$-$P_{out}$ channel:

$$S_{ED,mm2}^{SP} = \mathrm{Sin}[\theta]^2 (\chi_{zyy} \mathrm{Cos}[\phi]^2 + \chi_{zxx} \mathrm{Sin}[\phi]^2)^2. \quad (10)$$

In the $S_{in}$-$S_{out}$ channel:

$$S_{ED,mm2}^{SS} = 0. \quad (11)$$

3. **Bulk MD** under the point group ***mmm***:

The rank-3 nonlinear optical susceptibility tensor has the form:

$$\chi_{mmm}^{MD} = \begin{pmatrix} \begin{pmatrix} 0 \\ 0 \\ 0 \end{pmatrix} & \begin{pmatrix} 0 \\ 0 \\ \chi_{xyz} \end{pmatrix} & \begin{pmatrix} 0 \\ \chi_{xyz} \\ 0 \end{pmatrix} \\ \begin{pmatrix} 0 \\ 0 \\ \chi_{yxz} \end{pmatrix} & \begin{pmatrix} 0 \\ 0 \\ 0 \end{pmatrix} & \begin{pmatrix} \chi_{yxz} \\ 0 \\ 0 \end{pmatrix} \\ \begin{pmatrix} 0 \\ \chi_{zxy} \\ 0 \end{pmatrix} & \begin{pmatrix} \chi_{zxy} \\ 0 \\ 0 \end{pmatrix} & \begin{pmatrix} 0 \\ 0 \\ 0 \end{pmatrix} \end{pmatrix}, \quad (12)$$

leading to the following functional forms for the radiation.

In the $P_{in}$-$P_{out}$ channel:

$$S_{MD,mmm}^{PP} = 4\mathrm{Cos}[\theta]^2 \mathrm{Sin}[\theta]^2 (\mathrm{Cos}[\theta]^4 + \mathrm{Sin}[\theta]^4)(\chi_{yxz} \mathrm{Cos}[\phi]^2 - \chi_{xyz} \mathrm{Sin}[\phi]^2)^2. \quad (13)$$

In the $P_{in}$-$S_{out}$ channel:

$$S_{MD,mmm}^{PS} = (\chi_{xyz} + \chi_{yxz} - \chi_{zxy})^2 \mathrm{Cos}[\theta]^4 \mathrm{Sin}[\theta]^2 \mathrm{Sin}[2\phi]^2. \quad (14)$$

In the $S_{in}$-$P_{out}$ channel:

$$S_{MD,mmm}^{SP} = 0. \quad (15)$$

In the $S_{in}$-$S_{out}$ channel:

$$S^{SS}_{MD,mmm} = \chi^2_{zxy}\mathrm{Sin}[\theta]^2\mathrm{Sin}[2\phi]^2. \tag{16}$$

4. **EFISH** with induced electric dipole along the *c*-axis under the point group ***mmm***:

The rank-4 nonlinear optical susceptibility tensor has the form:

$$\chi^{EFISH}_{mmm} \tag{17}$$
$$= \left\{ \begin{array}{ccc} \begin{pmatrix} \chi_{xxxx} & 0 & 0 \\ 0 & \chi_{xxyy} & 0 \\ 0 & 0 & \chi_{xxzz} \end{pmatrix} & \begin{pmatrix} 0 & \chi_{xyxy} & 0 \\ \chi_{xxyy} & 0 & 0 \\ 0 & 0 & 0 \end{pmatrix} & \begin{pmatrix} 0 & 0 & \chi_{xzxz} \\ 0 & 0 & 0 \\ \chi_{xxzz} & 0 & 0 \end{pmatrix} \\ \begin{pmatrix} 0 & \chi_{yyxx} & 0 \\ \chi_{yxyx} & 0 & 0 \\ 0 & 0 & 0 \end{pmatrix} & \begin{pmatrix} \chi_{yyxx} & 0 & 0 \\ 0 & \chi_{yyyy} & 0 \\ 0 & 0 & \chi_{yyzz} \end{pmatrix} & \begin{pmatrix} 0 & 0 & 0 \\ 0 & 0 & \chi_{yzyz} \\ 0 & \chi_{yyzz} & 0 \end{pmatrix} \\ \begin{pmatrix} 0 & 0 & \chi_{zzxx} \\ 0 & 0 & 0 \\ \chi_{zxzx} & 0 & 0 \end{pmatrix} & \begin{pmatrix} 0 & 0 & 0 \\ 0 & 0 & \chi_{zzyy} \\ 0 & \chi_{zyzy} & 0 \end{pmatrix} & \begin{pmatrix} \chi_{zzxx} & 0 & 0 \\ 0 & \chi_{zzyy} & 0 \\ 0 & 0 & \chi_{zzzz} \end{pmatrix} \end{array} \right\},$$

leading to the following functional forms for the radiation.

In the $P_{in}$-$P_{out}$ channel:

$$\begin{aligned} S^{PP}_{EFISH,mmm} = {} & 4\mathrm{Cos}[\theta]^4\mathrm{Sin}[\theta]^2(\chi_{xzxz}\mathrm{Cos}[\phi]^2 + \chi_{yzyz}\mathrm{Sin}[\phi]^2)^2 \\ & + \mathrm{Sin}[\theta]^2(\chi_{zzzz}\mathrm{Sin}[\theta]^2 + \mathrm{Cos}[\theta]^2(\chi_{zxxz}\mathrm{Cos}[\phi]^2 \\ & + \chi_{zyyz}\mathrm{Sin}[\phi]^2))^2 \end{aligned} \tag{18}$$

In the $P_{in}$-$S_{out}$ channel:

$$S^{PS}_{EFISH,mmm} = 4(\chi_{xzxz} - \chi_{yzyz})^2\mathrm{Cos}[\theta]^2\mathrm{Cos}[\phi]^2\mathrm{Sin}[\theta]^2\mathrm{Sin}[\phi]^2 \tag{19}$$

In the $S_{in}$-$P_{out}$ channel:

$$S^{SP}_{EFISH,mmm} = \mathrm{Sin}[\theta]^2(\chi_{zyyz}\mathrm{Cos}[\phi]^2 + \chi_{zxxz}\mathrm{Sin}[\phi]^2)^2 \tag{20}$$

In the $S_{in}$-$S_{out}$ channel:

$$S^{SS}_{EFISH,mmm} = 0. \tag{21}$$

**Supplementary Note 5: domain survey on bulk CrSBr**

We have surveyed several locations on two pieces of bulk CrSBr samples. Supplementary Fig. 6a and 6b present the optical image of the two CrSBr samples. Supplementary Fig. 6c shows the SHG RA patterns measured in the $P_{in}$-$P_{out}$ channel at the locations numbered and labeled in Supplementary Fig. 6a and 6b. It can be noted that each of the CrSBr sample is a single domain.

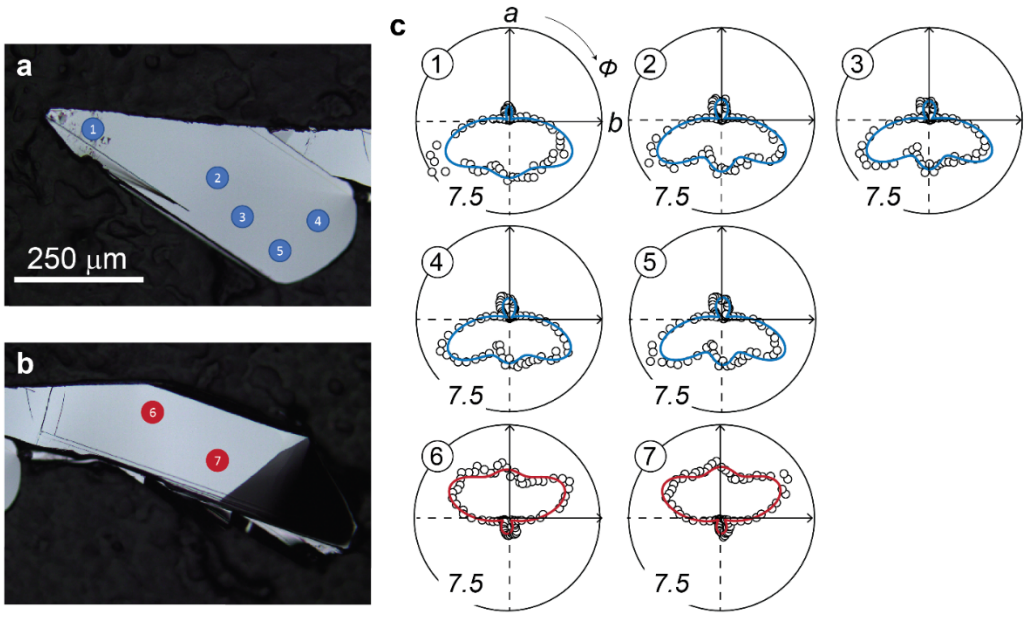


**Supplementary Fig. 6 | Spatial survey of magnetic domains of bulk CrSBr.** Optical image of **a**, sample 1 and **b**, sample 2. **c**, SHG RA in the $P_{in}$-$P_{out}$ channel measured at the locations numbered and labelled in **a** and **b**. Experiment data (circles) are fitted by functional forms simulated based on group theory analysis (solid curves). Numbers at the corners indicate the scales of the polar plots, with 1.0 corresponding to 1 fW.

We also surveyed the SHG RA patterns at the same location on the sample through multiple thermal cycles. Supplementary Fig. 7a shows the SHG RA patterns in the four polarization channels observed through the first cool down. After heating up to 185 K (Supplementary Fig. 7b) and cool down to 80 K again, a different set of SHG RA patterns are observed (Supplementary Fig. 7c). The patterns shown in Supplementary Fig. 7a and Supplementary Fig. 7c are related by $m_a$ and $C_{2c}$, which are the relations between the degenerate magnetic domains. This indicates that different magnetic domains are randomly selected through each thermal cycle. We have performed four thermal cycles, one of which shows the flip of the SHG RA patterns.

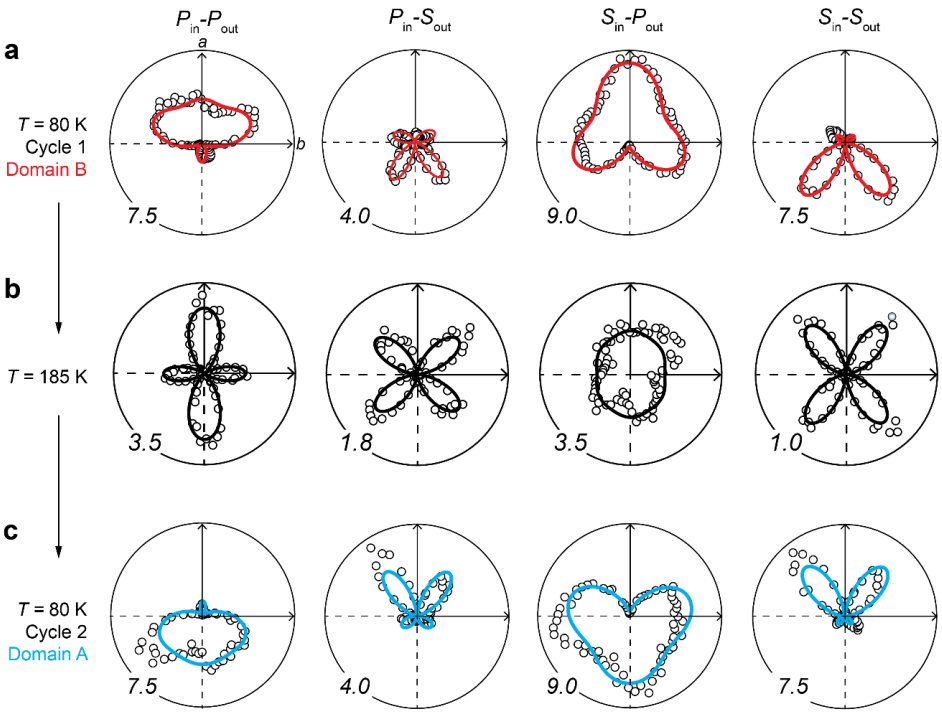


**Supplementary Fig. 7 | Magnetic domains of bulk CrSBr under different thermal cycles.** SHG RA patterns measured at the same location on the sample through multiple thermal cycles. Two sets of patterns, related by $m_a$ and $C_{2c}$, have been observed at 80 K, which come from **a**, domain B and **c**, domain A. **b**, SHG RA patterns measured at $T$ = 185 K. Experiment data (circles) are fitted by functional forms simulated based on group theory analysis (solid curves). Numbers at the corners indicate the scales of the polar plots, with 1.0 corresponding to 1 fW.

**Supplementary Note 6: superposition of surface ED and bulk EQ**

Here, we provide the functional forms of SHG radiation under the superposition of bulk EQ and surface ED. The nonlinear optical susceptibility tensor for bulk EQ has already been given in Supplementary Note 4. We now need to consider the time-variant (*c*-type) SHG radiation from the surface under the magnetic point group $\boldsymbol{m'm2'}$:

The rank-3 nonlinear optical susceptibility tensor has the form:

$$\chi_{m'm2'}^{ED,c,A} = \begin{pmatrix} \begin{pmatrix} \chi_{xxx} \\ 0 \\ 0 \end{pmatrix} & \begin{pmatrix} 0 \\ \chi_{xyy} \\ 0 \end{pmatrix} & \begin{pmatrix} 0 \\ 0 \\ \chi_{xzz} \end{pmatrix} \\ \begin{pmatrix} 0 \\ \chi_{yxy} \\ 0 \end{pmatrix} & \begin{pmatrix} \chi_{yxy} \\ 0 \\ 0 \end{pmatrix} & \begin{pmatrix} 0 \\ 0 \\ 0 \end{pmatrix} \\ \begin{pmatrix} 0 \\ 0 \\ \chi_{zxz} \end{pmatrix} & \begin{pmatrix} 0 \\ 0 \\ 0 \end{pmatrix} & \begin{pmatrix} \chi_{zxz} \\ 0 \\ 0 \end{pmatrix} \end{pmatrix} \tag{22}$$

for domain A, and

$$\chi_{m'm2'}^{ED,c,B} = \begin{pmatrix} \begin{pmatrix} -\chi_{xxx} \\ 0 \\ 0 \end{pmatrix} & \begin{pmatrix} 0 \\ -\chi_{xyy} \\ 0 \end{pmatrix} & \begin{pmatrix} 0 \\ 0 \\ -\chi_{xzz} \end{pmatrix} \\ \begin{pmatrix} 0 \\ -\chi_{yxy} \\ 0 \end{pmatrix} & \begin{pmatrix} -\chi_{yxy} \\ 0 \\ 0 \end{pmatrix} & \begin{pmatrix} 0 \\ 0 \\ 0 \end{pmatrix} \\ \begin{pmatrix} 0 \\ 0 \\ -\chi_{zxz} \end{pmatrix} & \begin{pmatrix} 0 \\ 0 \\ 0 \end{pmatrix} & \begin{pmatrix} -\chi_{zxz} \\ 0 \\ 0 \end{pmatrix} \end{pmatrix} \tag{23}$$

for domain B. Note that the rank-3 nonlinear optical susceptibility tensors for domain A and B are related by a minus sign because of the time-reversal relation, leading to the different interference patterns shown in Figure 4 of the main text. The radiation solely from the ***c*-type surface ED** under the magnetic point group $\boldsymbol{m'm2'}$ is:

In the $P_{in}$-$P_{out}$ channel:

$$S_{ED,m'm2'}^{PP} = \Big(-2\chi_{zxz}\mathrm{Cos}[\theta]\mathrm{Cos}[\phi]\mathrm{Sin}[\theta]^2 + \mathrm{Cos}[\theta]\Big(\chi_{xzz}\mathrm{Cos}[\phi]\mathrm{Sin}[\theta]^2 + \mathrm{Cos}[\theta]^2\big(\chi_{xxx}\mathrm{Cos}[\phi]^3 + (\chi_{xyy} + 2\chi_{yxy})\mathrm{Cos}[\phi]\mathrm{Sin}[\phi]^2\big)\Big)\Big)^2. \quad (24)$$

In the $P_{in}$-$S_{out}$ channel:

$$S_{ED,m'm2'}^{PS} = \Big(\chi_{xzz}\mathrm{Sin}[\theta]^2\mathrm{Sin}[\phi] + \mathrm{Cos}[\theta]^2\Big(\big(\chi_{xxx} - 2\chi_{yxy}\big)\mathrm{Cos}[\phi]^2\mathrm{Sin}[\phi] + \chi_{xyy}\mathrm{Sin}[\phi]^3\Big)\Big)^2. \quad (25)$$

In the $S_{in}$-$P_{out}$ channel:

$$S_{ED,m'm2'}^{SP} = \Big(\mathrm{Cos}[\theta]\big(\chi_{xyy}\mathrm{Cos}[\phi]^3 + \big(\chi_{xxx} - 2\chi_{yxy}\big)\mathrm{Cos}[\phi]\mathrm{Sin}[\phi]^2\big)\Big)^2. \quad (26)$$

In the $S_{in}$-$S_{out}$ channel:

$$S_{ED,m'm2'}^{SS} = \Big(\big(\chi_{xyy} + 2\chi_{yxy}\big)\mathrm{Cos}[\phi]^2\mathrm{Sin}[\phi] + \chi_{xxx}\mathrm{Sin}[\phi]^3\Big)^2. \quad (27)$$

Note that the SHG radiation from domain A and B share the same form. Only the interference between the surface magnetism and the bulk EQ radiations will lead to distinct patterns between domain A and domain B, as is shown below:

Considering the interference between surface **ED** with surface magnetism under the magnetic point group $\boldsymbol{m'm2'}$ and **EQ** under the point group $\boldsymbol{mmm}$:

In the $P_{in}$-$P_{out}$ channel:

$$S_{ED+EQ}^{PP} = (\mathrm{Sin}[\theta](-2\chi_{zxz}\mathrm{Cos}[\theta]\mathrm{Cos}[\phi]\mathrm{Sin}[\theta] - \chi_{zzzz}\mathrm{Cos}[\theta]\mathrm{Sin}[\theta]^2 - \mathrm{Cos}[\theta]^3(\chi_{zxzx}\mathrm{Cos}[\phi]^2 + \chi_{zyzy}\mathrm{Sin}[\phi]^2) + 2\mathrm{Cos}[\theta]\mathrm{Sin}[\theta]^2(\chi_{zzxx}\mathrm{Cos}[\phi]^2 + \chi_{zzyy}\mathrm{Sin}[\phi]^2)) + \mathrm{Cos}[\theta](\chi_{xzz}\mathrm{Cos}[\phi]\mathrm{Sin}[\theta]^2 + 2\mathrm{Cos}[\theta]^2\mathrm{Sin}[\theta](\chi_{xxzz}\mathrm{Cos}[\phi]^2 + \chi_{yyzz}\mathrm{Sin}[\phi]^2) - \mathrm{Sin}[\theta]^3(\chi_{xzxz}\mathrm{Cos}[\phi]^2 + \chi_{yzyz}\mathrm{Sin}[\phi]^2) + \mathrm{Cos}[\theta]^2(\chi_{xxx}\mathrm{Cos}[\phi]^3 + (\chi_{xyy} + 2\chi_{yxy})\mathrm{Cos}[\phi]\mathrm{Sin}[\phi]^2) - \mathrm{Cos}[\theta]^2\mathrm{Sin}[\theta](\chi_{xxxx}\mathrm{Cos}[\phi]^4 + (2\chi_{xxyy} + \chi_{xyxy} + \chi_{yxyx} + 2\chi_{yyxx})\mathrm{Cos}[\phi]^2\mathrm{Sin}[\phi]^2 + \chi_{yyyy}\mathrm{Sin}[\phi]^4)))^2. \quad (28)$$

In the $P_{in}$-$S_{out}$ channel:

$$S_{ED+EQ}^{PS} = (2(\chi_{xxzz} - \chi_{yyzz})\mathrm{Cos}[\theta]^2\mathrm{Cos}[\phi]\mathrm{Sin}[\theta]\mathrm{Sin}[\phi] + \chi_{xzz}\mathrm{Sin}[\theta]^2\mathrm{Sin}[\phi] - (\chi_{xzxz} - \chi_{yzyz})\mathrm{Cos}[\phi]\mathrm{Sin}[\theta]^3\mathrm{Sin}[\phi] + \mathrm{Cos}[\theta]^2((\chi_{xxx} - 2\chi_{yxy})\mathrm{Cos}[\phi]^2\mathrm{Sin}[\phi] + \chi_{xyy}\mathrm{Sin}[\phi]^3) - \mathrm{Cos}[\theta]^2\mathrm{Sin}[\theta]((\chi_{xxxx} - \chi_{yxyx} - 2\chi_{yyxx})\mathrm{Cos}[\phi]^3\mathrm{Sin}[\phi] + (2\chi_{xxyy} + \chi_{xyxy} - \chi_{yyyy})\mathrm{Cos}[\phi]\mathrm{Sin}[\phi]^3))^2. \quad (29)$$

In the $S_{in}$-$P_{out}$ channel:

$$S_{ED+EQ}^{SP} = (-\mathrm{Cos}[\theta]\mathrm{Sin}[\theta](\chi_{zyzy}\mathrm{Cos}[\phi]^2 + \chi_{zxzx}\mathrm{Sin}[\phi]^2) + \mathrm{Cos}[\theta](\chi_{xyy}\mathrm{Cos}[\phi]^3 + (\chi_{xxx} - 2\chi_{yxy})\mathrm{Cos}[\phi]\mathrm{Sin}[\phi]^2 - \mathrm{Sin}[\theta](\chi_{xyxy}\mathrm{Cos}[\phi]^4 + (\chi_{xxxx} - 2(\chi_{xxyy} + \chi_{yyxx}) + \chi_{yyyy})\mathrm{Cos}[\phi]^2\mathrm{Sin}[\phi]^2 + \chi_{yxyx}\mathrm{Sin}[\phi]^4)))^2. \quad (30)$$

In the $S_{in}$-$S_{out}$ channel:

$$S_{ED+EQ}^{SS} = ((\chi_{xyy} + 2\chi_{yxy})\mathrm{Cos}[\phi]^2\mathrm{Sin}[\phi] + \chi_{xxx}\mathrm{Sin}[\phi]^3 - \mathrm{Sin}[\theta]((\chi_{xyxy} + 2\chi_{yyxx} - \chi_{yyyy})\mathrm{Cos}[\phi]^3\mathrm{Sin}[\phi] + (\chi_{xxxx} - 2\chi_{xxyy} - \chi_{yxyx})\mathrm{Cos}[\phi]\mathrm{Sin}[\phi]^3))^2 \quad (31)$$

for domain A. Domain B shares the similar functional forms with an additional minus sign before all the rank-3 tensor elements $\chi_{ijk}$.

**Supplementary Note 7: thickness dependent SHG measurements**

The symmetry analysis discussed in the last section is the primary criterion to distinguish the surface and bulk contributions to SHG. Besides, we performed thickness dependent SHG RA at 80 K as a secondary check to confirm the surface ED SHG origin from the surface AFM order. We investigated three different thickness, 160nm, 450nm, and 7500nm (7.5 μm) that are quantified by the atomic force microscopy measurements. In Supplementary Fig. 8, we show their SHG RA patterns in the $S_{in}$-$S_{out}$ channel and their decomposition into the bulk EQ and surface ED contributions. We can clearly see that:

a) As the thickness increases, the surface ED SHG contribution stays nearly the same. This is consistent with its surface nature.
b) In contrast, when the thickness increases, the bulk EQ SHG contribution increases which is also consistent with its bulk nature. From the trend, we can also roughly estimate our light penetration depth is slightly deeper than 450nm.

With the confirmation of the surface origin of SHG that onsets at $T_s$ = 140 K, we are confident about our assignment of the surface layered AFM order.

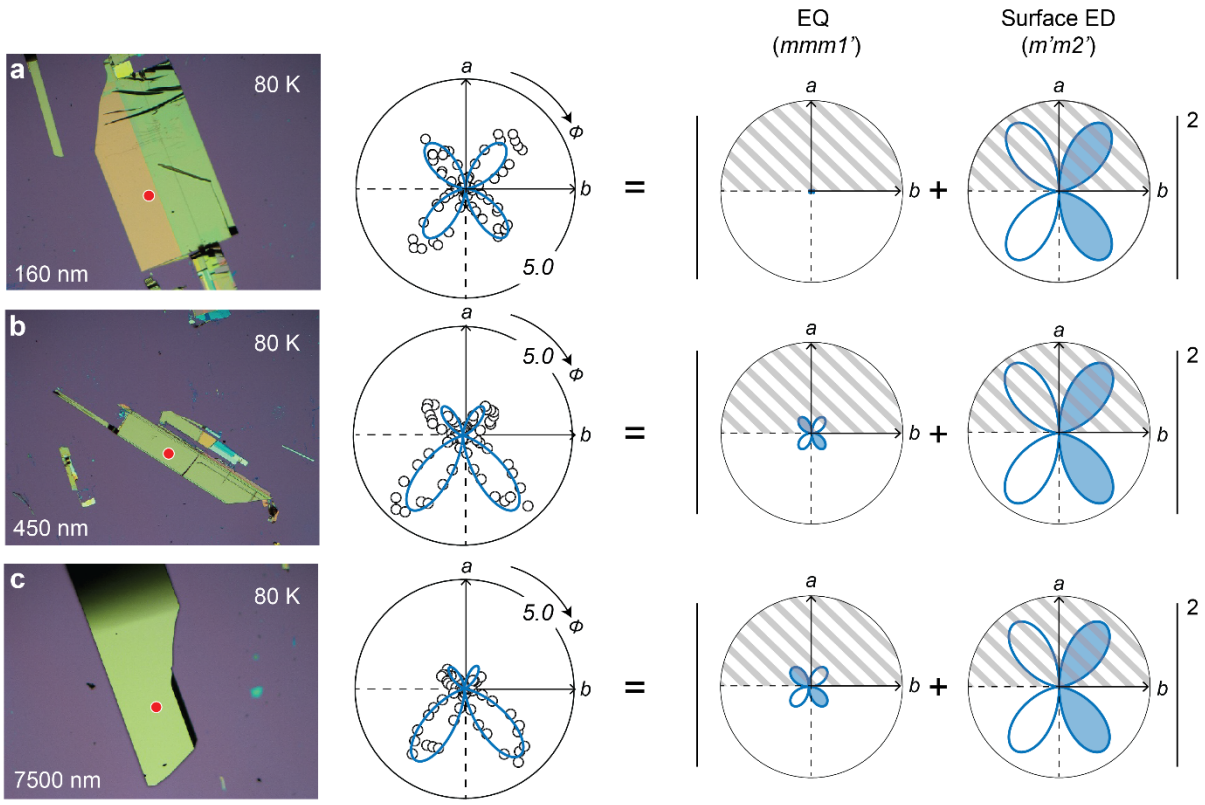


**Supplementary Fig. 8 | Thickness dependent SHG RA.** Optical image, bulk EQ and surface ED SHG contributions in the $S_{in}$-$S_{out}$ channel and their interference for samples with thickness **a**. 160 nm **b**. 450 nm and **c**. 7500 nm. All the patterns are measured at 80 K. Red dots in the optical images indicate the location for SHG measurements. Experiment data (circles) are fitted by functional forms simulated based on group theory analysis (solid curves). Numbers at the corners indicate the scales of the polar plots, with 1.0 corresponding to 1 fW. EQ: electric quadrupole, ED: electric dipole.

**Supplementary Note 8: SHG RA measured in sequence of time**

We prove the stability of our system by showing the consistency of RA SHG data taken at the same temperature but 45 minutes apart. Supplementary Fig. 9 shows four RA SHG patterns taken every 15 min in the $P_{in}$-$P_{out}$ channel at 130 K. Within our technique sensitivity, there are no observable changes in the measured patterns, indicating the system is in its equilibrium state.

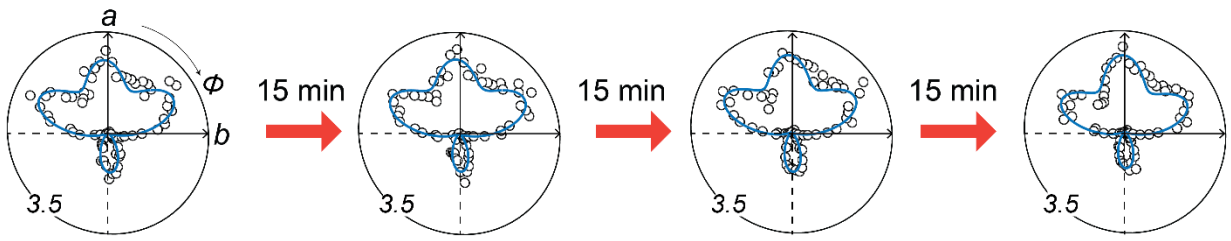


**Supplementary Fig. 9 |** SHG RA patterns taken every 15 min in the $P_{in}$-$P_{out}$ channel at 130 K. No observable changes are detected, indicating the system is in its equilibrium state. Experiment data (circles) are fitted by functional forms simulated based on group theory analysis (solid curves). Numbers at the corners indicate the scales of the polar plots, with 1.0 corresponding to 1 fW.

**Supplementary Note 9: temperature dependence of $C_2^{ED}$ and $D_2^{ED}$**

The $C_2^{ED} = \chi_{xxx}$ and $D_2^{EQ} = \chi_{xyxy} + 2\chi_{yyxx} - \chi_{yyyy}$ fitted from the temperature-dependent SHG RA in the $S_{in}$-$S_{out}$ channel are plotted in Supplementary Fig. 10. Both $C_2^{ED}$ and $D_2^{EQ}$ have a relatively large uncertainty. Despite this, $D_2^{EQ}$ is capable of tracking $T^{**}$ and $T_S$, similar as $D_1^{EQ}$ in the Fig. 5c of the main text. However, unlike $D_1^{EQ}$, $D_2^{EQ}$ cannot capture $T_N$ due to the larger uncertainty.

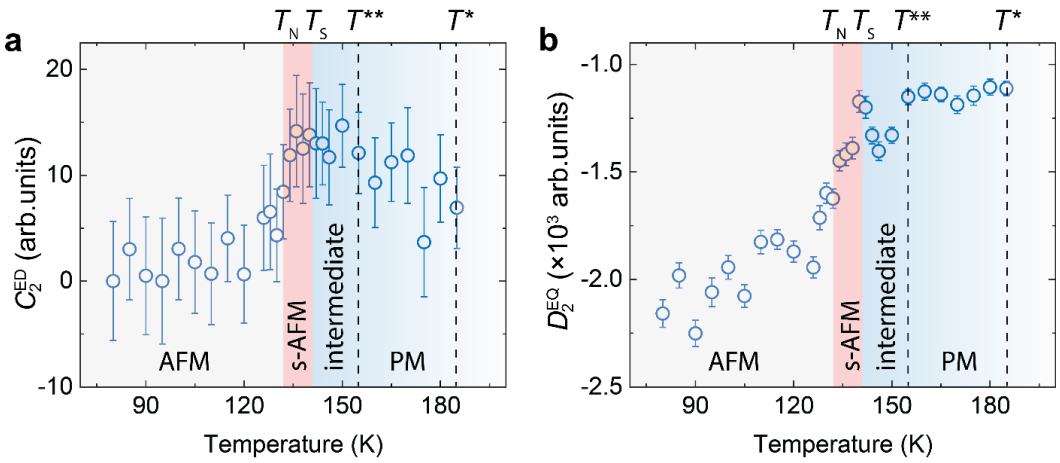


**Supplementary Fig. 10 | Temperature dependence of $C_2^{ED}$ and $D_2^{EQ}$.** **a**, $C_2^{ED}$ and **b**, $D_2^{EQ}$ as a function of temperature fitted from the $S_{in}$-$S_{out}$ channel. The regions of paramagnetism (PM), intermediate magnetic crossover (intermediate), surface antiferromagnetism (s-AFM) and bulk antiferromagnetism (AFM) are shaded in different colors, with their characteristic temperatures marked. Error bars indicate the standard deviations from the fitting.

**Supplementary Note 10: SHG and magnetization measurements from multiple samples**

We performed the same SHG RA measurements and analysis on a sample prepared separately (referred as Sample 2). We also performed the fit of the temperature dependence of the electric dipole (ED) susceptibility tensor elements, using the functional form of $C_1^{ED} = A\,(T_s - T)^{\beta} + B$ for $T < T_s$ and $C_1^{ED} = B$ for $T \geq T_s$. Due to the kink at $T_N$ = 132 K known as the impact on the surface order by the bulk order, we limit our fit to the data between the temperature range of 132 K – 200 K. For our two independent RA SHG measurements on two samples, the fitted surface onset temperatures are $T_S$ = 140 ± 0.2K (Sample 1, sample for the main text Figure 5) and 140 ± 0.1 K (Sample 2), respectively (see Supplementary Figs. 11a and 11c). The critical exponent, $\beta$, varies dramatically between different temperature ranges for fitting, being $\beta$ = 0.6 ± 0.2 for Sample 1 and 0.4 ± 0.1 for Sample 2. Such a variation in $\beta$ is due to the lack of data points between 132 K and 140 K and also the impact of the bulk onset at 132 K. The error represents the 95% confidence interval calculated from the standard deviations given by the fitting process. In addition, we note that the temperature dependent ED signals show a notable kink (i.e., change of curvature) near $T_N$ = 132 K for both measurements, which is consistent with the expectation/prediction that the bulk order at $T_N$ = 132 K impacts the surface order.

Furthermore, we performed the temperature dependent magnetization measurements on Sample 1 and another sample from the same batch of Sample 2. For both samples, we can clearly see the bulk transition temperature at $T_N$ = 132 ± 1 K (see Supplementary Figs. 11b and 11d). Our bulk magnetism onset temperature is consistent with the literature values for bulk single crystal CrSBr.

With these results, we are confident about our finding of two phase transitions happening in 3D bulk CrSBr, a surface phase transition at $T_S$ = 140 ± 0.2 K and a bulk ordering onset at $T_N$ = 132 ± 1 K.

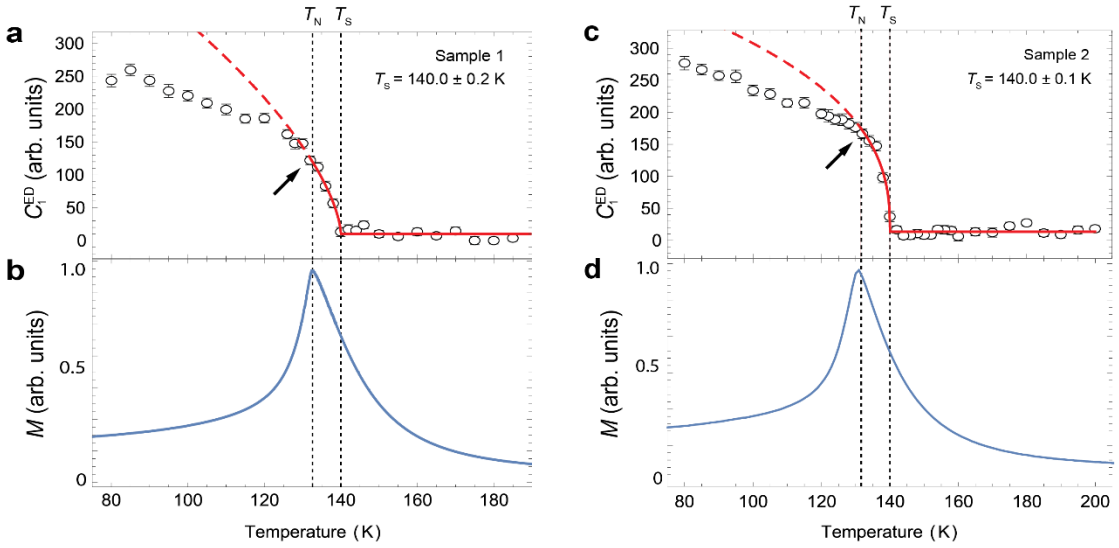


**Supplementary Fig. 11 | Observation of enhanced surface magnetic transition temperatures in multiple samples.** Surface ED SHG coefficient $C_1^{ED}$ and magnetization $M$ as a function of temperature measured from sample 1 (**a** and **b**) and sample 2 (**c** and **d**). The extracted transition temperatures are also labelled. Red curves show the best order-parameter fit using data for $T > 132$ K. Black arrows indicate the kinks at $T_N = 132$ K. Error bars are standard deviations from the fitting.

**Supplementary Note 11: assignment of crossover at the temperature scale $T^{**}$ = 155 K**

Our revised interpretation for $T^{**}$ = 155 K is a temperature scale, below which the spin forms fluctuating, short-ranged patches within and between *ab*-planes for the entire bulk. Within each patch, the spins on average align along the *b*-axis direction (Supplementary Fig. 12a). Then, below $T_S$ = 140 K, the surface layers order in the layered AFM state whereas the deeper bulk remains in the fluctuating, short-ranged form (Supplementary Fig. 12b). And finally, below $T_N$ = 132K, the entire sample enters the layered AFM state (Supplementary Fig. 12c). The reasons for this revised assignment are listed as follows:

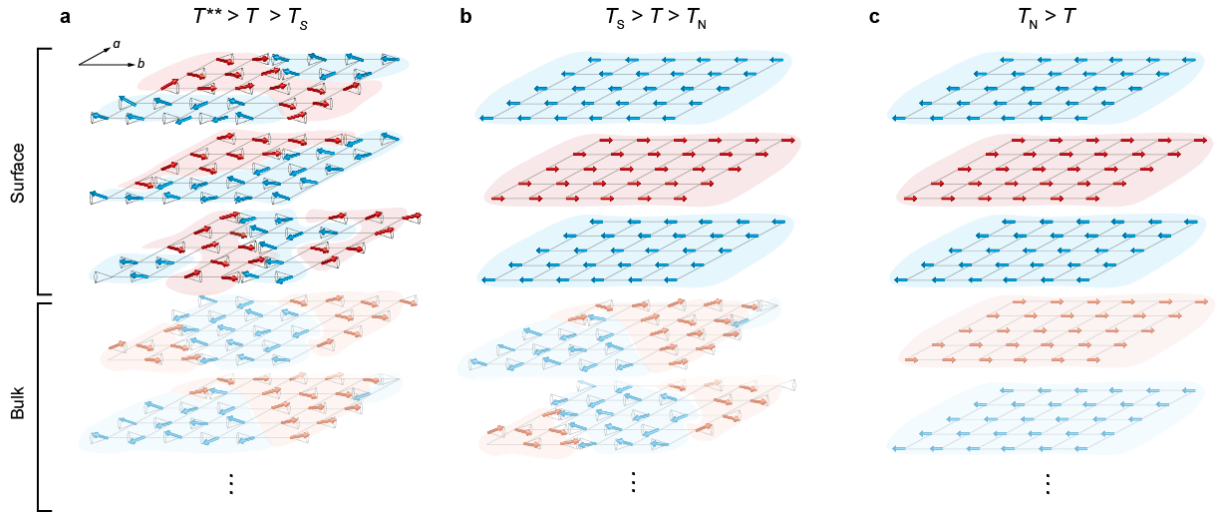


**Supplementary Fig. 12 | Proposed spin texture at various temperatures. a**. At $T^{**} > T > T_S$ the whole sample develops a multi-patch state with short-range correlations. **b**. At $T_S > T > T_N$, the surface develops layered AFM order, whereas the bulk still only has short-range correlations. **c**. $T < T_N$, a long-range layered AFM order is developed across the sample.

1) We observed both $T^{**}$ = 155 K and $T_S$ = 140 K, in addition to $T_N$ = 132 K, in the temperature dependent SHG RA data (Figures 5b and 5c of the main text). If the spins form the ferromagnetic long-range order within the *ab*-plane below $T^{**}$ = 155 K, we can ask what changes in SHG RA would be upon the formation of this state. From the symmetry perspective, the surface magnetic point group of this *c*-axis incoherent magnetic state is *m'm2'*, and the bulk magnetic point group is *mmm1'*. Due to the in-plane long-range order, we would anticipate the surface ED contribution and the bulk EQ contribution to SHG RA right below $T^{**}$ = 155K. In addition, due to the *c*-axis incoherence, its surface magnetic state has $2^N$ options,

where $N$ is the layer number for surface magnetism, and therefore we would expect $2^N$ degenerate domain states. However, right below $T^{**}$ = 155 K (above $T_S$ = 140 K), we don't observe surface ED SHG in our data and only find one type of SHG RA between $T^{**}$ and $T_S$. This distinction between our expectation of SHG RA for the *c*-axis incoherent state and the observed SHG RA between $T^{**}$ and $T_S$ motivates us to consider a different possibility of the magnetic state between $T^{**}$ and $T_S$ from the "intralayer order" with *c*-axis incoherence.

2) At the same time, our proposed picture of fluctuating, short-ranged patches with an average spin alignment along the *b*-axis inside patches is consistent with our experimental data. As there is no global symmetry breaking either at the surface or inside the bulk, we don't observe changes in RA SHG patterns across $T^{**}$. But because there is an average effect to make the *b*-axis slightly different from the *a*-axis throughout the sample, we do observe in the bulk EQ SHG that the susceptibility tensor element amplitudes change.
3) We find the transition from the *c*-axis incoherent "intralayer order" to the layered AFM order is unlikely to happen at $T_N$ = 132 K for bulk CrSBr. Between these two states, the energy gain is in the order of $\Delta E \sim nNJ$, where $J$ is the interlayer AFM exchange coupling, $n$ is the number of interlayer bond per two neighboring layers, and $N$ is the number of layers for a bulk sample. And between these two states, the entropy reduction is $\Delta S \sim k_B N \ln 2$, as the number of possible states reduces from $2^N$ to 2. A thermodynamic phase transition can happen when $\Delta E = T_c \Delta S$, leading to a critical temperature of $T_c = \frac{nJ}{k_B}$. For the intralayer long range orders, $n \to \infty$ and therefore $T_c \to \infty$, rather than the finite temperature of $T_N$ = 132 K. Therefore, it is unlikely that the bulk magnetic state is the *c*-axis incoherent "intralayer order" below 155 K.

With these considerations, we assign the observed temperature scale of $T^{**}$ = 155 K to be a crossover temperature scale for the system to enter a state with fluctuating, short-ranged patches of spins that on average align with the *b*-axis within individual patches.

**Supplementary Note 12: supplementary results from density functional theory (DFT) calculation**

Supplementary Fig. 13 shows the $U$-dependence of $J_6$, which hardly changes from bulk to monolayer CrSBr under various settings.

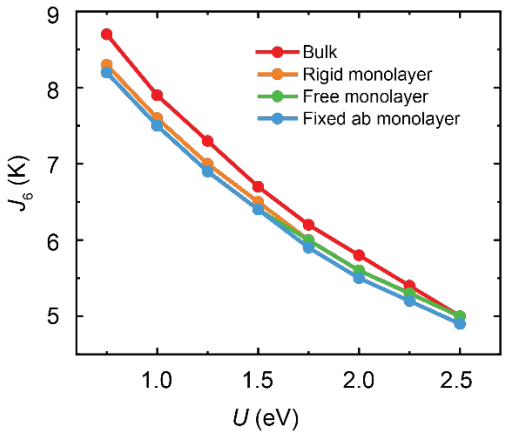


**Supplementary Fig. 13 |** $U$-dependence of $J_6$ for bulk CrSBr (red), rigid monolayer (orange), fixed *ab* monolayer (blue) and free monolayer (green).

Supplementary Table 1 provides the information from $J_1$ to $J_7$ and the Curie-Weiss temperatures in bulk CrSBr and monolayer CrSBr under various settings. The corresponding Cr-Cr distance for each $J$ has also been provided.

**Supplementary Table 1.** Energy mapping results for CrSBr bulk and monolayers

bulk

| $U$ (eV) | $J_1$ | $J_2$ | $J_3$ | $J_4$ | $J_5$ | $J_6$ | $J_7$ | $\vartheta_{\mathrm{CW}}$ |
|---|---|---|---|---|---|---|---|---|
| 0.75 | -7.7(8) | -37.7(7) | -31.7(3) | -0.4(7) | 0.2(7) | 8.7(4) | -2.4(2) | 278.1 |
| 1.0 | -12.1(7) | -38.9(6) | -30.2(3) | -0.4(6) | 0.1(6) | 7.9(4) | -2.3(2) | 293.8 |
| 1.25 | -15.8(6) | -39.9(5) | -28.7(3) | -0.5(5) | 0.1(5) | 7.3(3) | -2.3(2) | 306.1 |
| 1.5 | -19.1(6) | -40.6(5) | -27.3(2) | -0.5(5) | 0.1(5) | 6.7(3) | -2.3(2) | 315.9 |
| 1.75 | -21.9(5) | -41.1(4) | -26.0(2) | -0.5(4) | 0.1(4) | 6.2(3) | -2.2(2) | 323.4 |
| 2.0 | -24.5(5) | -41.5(4) | -24.8(2) | -0.5(4) | 0.1(4) | 5.8(2) | -2.2(2) | 329.3 |
| 2.25 | -26.7(4) | -41.7(4) | -23.6(2) | -0.5(4) | 0.1(4) | 5.4(2) | -2.1(1) | 333.9 |
| 2.5 | -28.7(4) | -41.8(3) | -22.5(2) | -0.5(3) | 0.1(3) | 5.0(2) | -2.1(1) | 337.3 |
| $d_{\mathrm{Cr-Cr}}$ (Å) | 3.544 | 3.592 | 4.738 | 5.917 | 6.166 | 7.089 | 7.603 | |

rigid monolayer

| $U$ (eV) | $J_1$ | $J_2$ | $J_3$ | $J_4$ | $J_5$ | $J_6$ | $J_7$ | $\vartheta_{\mathrm{CW}}$ |
|---|---|---|---|---|---|---|---|---|
| 0.75 | -8.7(8) | -38.7(7) | -31.5(3) | -0.5(7) | -0.1(7) | 8.3(4) | -2.4(2) | 288.1 |
| 1.0 | -13.0(7) | -40.0(6) | -30.1(3) | -0.6(6) | -0.1(6) | 7.6(4) | -2.3(2) | 303.5 |
| 1.25 | -16.7(6) | -40.9(5) | -28.7(3) | -0.6(5) | -0.1(5) | 7.0(3) | -2.3(2) | 315.6 |
| 1.5 | -20.0(6) | -41.6(5) | -27.4(2) | -0.6(5) | -0.1(5) | 6.5(3) | -2.2(2) | 325.1 |
| 1.75 | -22.9(5) | -42.1(4) | -26.2(2) | -0.6(4) | -0.1(4) | 6.0(3) | -2.2(2) | 332.5 |
| 2.0 | -25.4(5) | -42.5(4) | -25.0(2) | -0.6(4) | 0.0(4) | 5.6(2) | -2.2(2) | 338.0 |
| 2.25 | -27.7(4) | -42.7(4) | -23.9(29 | -0.6(4) | 0.0(4) | 5.3(2) | -2.1(1) | 342.5 |
| 2.5 | -29.7(4) | -42.8(3) | -22.8(2) | -0.5(3) | 0.0(3) | 5.0(2) | -2.1(1) | 345.8 |
| $d_{\mathrm{Cr-Cr}}$ (Å) | 3.544 | 3.592 | 4.738 | 5.917 | 6.166 | 7.089 | 7.603 | |

free monolayer

| $U$ (eV) | $J_1$ | $J_2$ | $J_3$ | $J_4$ | $J_5$ | $J_6$ | $J_7$ | $\vartheta_{\mathrm{CW}}$ |
|---|---|---|---|---|---|---|---|---|
| 0.75 | -5.4(8) | -40.7(7) | -34.2(3) | -0.8(7) | -0.2(7) | 8.2(4) | -2.0(2) | 296.8 |
| 1.0 | -9.9(7) | -41.7(6) | -32.7(3) | -0.8(6) | -0.1(6) | 7.5(4) | -1.9(2) | 310.9 |
| 1.25 | -13.8(6) | -42.5(5) | -31.3(3) | -0.9(5) | -0.1(5) | 6.9(3) | -1.9(2) | 322.5 |
| 1.5 | -17.3(6) | -43.0(5) | -29.9(2) | -0.8(5) | -0.1(5) | 6.4(3) | -1.9(2) | 331.3 |
| 1.75 | -20.3(5) | -43.4(4) | -28.6(2) | -0.8(4) | 0.0(4) | 6.0(3) | -1.9(2) | 337.5 |
| 2.0 | -23.0(5) | -43.5(4) | -27.3(2) | -0.7(4) | 0.0(4) | 5.6(2) | -1.9(2) | 342.6 |
| 2.25 | -25.4(4) | -43.6(4) | -26.2(2) | -0.7(4) | 0.1(4) | 5.3(2) | -1.9(1) | 346.4 |
| 2.5 | -27.5(4) | -43.5(3) | -25.1(2) | -0.7(3) | 0.1(3) | 5.0(2) | -1.9(1) | 348.8 |
| $d_{\mathrm{Cr-Cr}}$ (Å) | 3.533 | 3.597 | 4.727 | 5.901 | 6.156 | 7.066 | 7.591 | |

fixed $ab$ monolayer

| $U$ (eV) | $J_1$ | $J_2$ | $J_3$ | $J_4$ | $J_5$ | $J_6$ | $J_7$ | $\vartheta_{\mathrm{CW}}$ |
|---|---|---|---|---|---|---|---|---|
| 0.75 | -9.1(8) | -40.1(7) | -34.0(3) | -0.7(7) | -0.1(7) | 8.2(4) | -2.1(2) | 302.4 |
| 1.0 | -13.3(7) | -41.2(6) | -32.5(3) | -0.7(6) | -0.1(6) | 7.5(4) | -2.0(2) | 316.5 |
| 1.25 | -17.0(6) | -42.0(5) | -31.0(3) | -0.8(5) | -0.1(5) | 6.9(3) | -2.0(2) | 327.3 |
| 1.5 | -20.2(6) | -42.6(5) | -29.6(2) | -0.7(5) | -0.1(5) | 6.4(3) | -2.0(2) | 335.7 |
| 1.75 | -23.1(5) | -42.9(4) | -28.3(2) | -0.7(4) | -0.1(4) | 5.9(3) | -2.0(2) | 342.3 |
| 2.0 | -25.6(5) | -43.1(4) | -27.0(2) | -0.7(4) | 0.0(4) | 5.5(2) | -2.0(2) | 347.0 |
| 2.25 | -27.9(4) | -43.2(4) | -25.9(2) | -0.7(4) | 0.0(4) | 5.2(2) | -2.0(1) | 350.4 |
| 2.5 | -29.8(4) | -43.2(3) | -24.7(2) | -0.6(3) | 0.1(3) | 4.9(2) | -1.9(1) | 352.9 |
| $d_{\mathrm{Cr-Cr}}$ (Å) | 3.544 | 3.599 | 4.738 | 5.917 | 6.171 | 7.089 | 7.606 | |

Supplementary Table 2 provides the information of the change in the interatomic distances and bond angles in bulk CrSBr and monolayer CrSBr under different settings.

**Supplementary Table 2.** Geometrical parameters for the three most important exchange paths of CrSBr

| $J_1$ | bulk | fixed $ab$ monolayer | free monolayer | rigid monolayer |
|---|---|---|---|---|
| Cr-Cr distance (Å) | 3.54428 | 3.54428 (±0%) | 3.53296 (-0.32%) | 3.54428 (±0%) |
| Cr-S distance (Å) | 2.39300 | 2.39200 (-0.04%) | 2.39051 (-0.10%) | 2.39295 (-0.00%) |
| Cr-S-Cr angle (°) | 95.5568 | 95.6096 (+0.06%) | 95.2852 ( -0.28%) | 95.5596 (-0.00%) |
| Cr-Br distance (Å) | 2.51795 | 2.52227 (+0.17%) | 2.52066 (+0.11%) | 2.51800 (+0.00%) |
| Cr-Br-Cr angle (°) | 89.4660 | 89.2714 (-0.22%) | 88.9827 (-0.54%) | 89.4634 (-0.00%) |

| $J_2$ | bulk | fixed $ab$ monolayer | free monolayer | rigid monolayer |
|---|---|---|---|---|
| Cr-Cr distance (Å) | 3.59191 | 3.59947 (+0.21%) | 3.59704 (+0.14%) | 3.59182 (-0.00%) |
| Cr-S distance (Å) | 2.40750 | 2.41018 (+0.11%) | 2.40521 (-0.10%) | 2.40749 (-0.00%) |
| Cr-S-Cr angle (°) | 96.8750 | 97.1018 (+0.23%) | 97.1894 (+0.32%) | 96.8736 (-0.00%) |

| $J_3$ | bulk | fixed $ab$ monolayer | free monolayer | rigid monolayer |
|---|---|---|---|---|
| Cr-Cr distance (Å) | 4.73800 | 4.73800 (±0%) | 4.72671 (-0.24%) | 4.73800 (±0%) |
| Cr-S distance (Å) | 2.40750 | 2.41018 (+0.11%) | 2.40521 (-0.10%) | 2.40749 (-0.00%) |
| Cr-S-Cr angle (°) | 159.4781 | 158.7861 (-0.43%) | 158.5902 (-0.56%) | 159.4818 (+0.00%) |